Jet energy loss with finite-size effects and running coupling in MARTINI

Chanwook Park

Master of Science

Department of Physics

McGill University

Montréal, Québec

August 2015

A Thesis submitted to the McGill University Faculty of Graduate Studies and Research in partial fulfillment of the requirements for the degree of Master of Science

DEDICATION

In dedication to my parents.

ACKNOWLEDGEMENTS

First and foremost, I would like to express my respectful gratitude to my supervisor, Prof. Sangyong Jeon, for his great kindness and patience. He has given me lots of support and guided me to the right direction of learning during my master's study. I would also like to thank Prof. Charles Gale for providing crucial advice at our group meetings. I am thankful to Sangwook Ryu who instructed me in the use of programs for my research and kindly help me to resolve all sort of issues concerning them. I feel grateful to Björn Schenke and Clint Young, as developers of MARTINI, from whom I could obtain detailed and essential information on the program.

I should also mention many thanks to my colleagues — Dr. Gabriel Denicol, Chun Shen, Gojko Vujanovic, Jean-Françis Paquet, Michael Richard, Igor Kozlov, and Scott McDonald — for not only discussions on physics but also helpful conversations about living in Montreal. I appriciate the professors who taught me the graduate courses in the Physics Department. Thanks to their dedicated teaching, it was possible for me to acquire comprehensive knowledge of my study. Finally, I owe a special thank to Yuri Oh who kindly proofread this thesis.

ABSTRACT

The suppression of jet production in heavy ion collisions is a sign of the creation of the hot and dense medium where quarks and gluons are deconfined. A number of phenomenological and theoretical descriptions have been proposed to address jet energy loss mechanisms in the QCD medium. In this thesis, we focus on the radiative energy loss and, following individual proposals by Caron-Huot and Gale [1] and Young, Schenke, Jeon, and Gale [2], study the finite formation time of a splitting process and the running effect of the strong coupling in an emission vertex. We utilize a Monte Carlo event generator, MARTINI (Modular Algorithm for Relativistic Treatment of heavy IoN Interactions), in which the two radiative energy loss models are incorporated. Using MARTINI, we compute jet quenching observables in PbPb collisions at $\sqrt{s} = 2.76$TeV using the ideal $(3 + 1)$ dimensional hydrodynamics background. We obtain a good description of charged particle R_{AA} at different centrality classes with a gradual rise up to 100GeV. Also we present distributions of dijet imbalance A_J compared to experimental measurements from the CMS. These results suggest that the two models play an significant role in the radiative energy loss. Finally, we discuss possibilities for improvement of this study by expanding the kinematic domain into that of the recent LHC energy scale and by applying more realistic hydrodynamical descriptions for the background medium.

ABRÉGÉ

La suppression de la production de jets dans les collisions d'ions lourds est un signe de la création de la matière chaude et dense où les quarks et les gluons sont déconfinés. Un certain nombre de descriptions phénoménologiques et théoriques ont été proposés afin d'aborder les mécanismes de perte d'énergie des jets dans les états de la QCD. Dans cette thèse, nous nous concentrons sur la perte d'énergie par rayonnement et nous étudions le temps de formation finie d'un processus de fractionnement ainsi que l'effet en cours d'exécution du couplage fort dans un sommet d'émission, suivant les propositions individuelles de Caron-Huot et Gale [1] et de Young, Schenke, Jeon, et Gale [2]. Nous utilisons un générateur d'événement de Monte-Carlo, MARTINI (Modular Algorithm for Relativistic Treatment of heavy IoN Interactions), dans lequel les deux modèles de perte d'énergie par rayonnement sont incorporés. À l'aide du MARTINI, nous calculer observables de jet trempe dans des collisions plomb-plomb à $\sqrt{s} = 2.76$TeV en utilisant l'arrière-plan idéal de $(3 + 1)$-dimensionnelle hydrodynamique. Nous obtenons une bonne description de la particule R_{AA} chargée à différentes classes de centralité jusqu'à une augmentation graduelle de 100GeV. Aussi, nous présentons la répartition des dijet déséquilibre A_J que nous avons comparée aux mesures expérimentales du CMS. Ces résultats suggèrent que les deux modèles jouent un rôle important dans la perte d'énergie par rayonnement. Enfin, nous discutons des possibilités pour améliorer cette étude en élargissant le domaine de la cinématique dans celui de l'échelle d'énergie récente LHC

et en appliquant des descriptions hydrodynamiques plus réalistes pour la matière de QGP.

TABLE OF CONTENTS

LIST OF TABLES

LIST OF FIGURES

CHAPTER 1
Introduction

1.1 Historical View of Heavy Ion Collision

The physics of a strongly coupled hot and dense medium, which explores dynamics of the very early universe, has been of great interest to subatomic physicists. In the last several decades, great efforts have been made in establishing the conceptual basis of the subject. This led us to a good understanding of the state of matter created under extreme conditions where quarks and gluons are deconfined.

Powerful accelerators, such as the Large Hadron Collider (LHC) and the Relativistic Heavy Ion Collider (RHIC), are the most important means of producing the quark-gluon plasma, QGP — the deconfined state of quarks and gluons. It is believed to have existed less than $\leq 20\mu s$ after the Big Bang. These facilities perform high-energy collisions between relativistic heavy ions during which exceedingly high temperatures and energy densities are achieved to create the QGP. In the early 21st century, the existence of the QGP was discovered through heavy-ion collision experiments, and the energy density in the QGP was estimated to be about 5GeV/fm^3. This achievement, however, posed a puzzling question. The discovered QGP medium behaved like a nearly perfect relativistic fluid, although a behaviour closer to an ideal gas was expected because quantum chromodynamics (QCD) features asymptotic freedom. Consequently, various attempts were made to describe the dynamics of the QCD medium and its space-time evolution in heavy ion collisions within the framework of hydrodynamics [4–6].

The discovery of the QGP has provided us with an opportunity to analyze the liquid-like extreme state of matter. Moreover, methodological development for the relativistic heavy ion collision experiments made it possible to collect valuable pieces of information on the exotic medium. The heavy ion programs, for instance, at the LHC with a highly increased energy scale of collisions facilitated the access to an enlarged kinematic regime of observables with a significant improvement in systematic reliability.

One of the most notable results from the LHC and RHIC is that a strong suppression of high transverse momentum (p_T) jets occurs in the QGP medium created in heavy ion collisions. A jet, one of main observables of collision experiments, is a highly collimated shower of particles concentrated in a small angular cone that are produced in hard scattering processes. Since these hard scatterings occur at the early stage of collisions before the QGP is created, these jets have a full history of soft interactions with the QGP medium. The interactions between the jets and the background medium result in a loss of jet energies as they propagate in the medium. This suppression, also known as jet quenching, has been studied indirectly by measuring hadronic-level observables such as leading hadron p_T spectra and azimuthal di-hadron correlations. An obvious clue of the quenched-jet phenomenon was revealed by referring to calibrated measurements of the identical observables in proton-proton collisions, in which the hot and dense medium is absent. Recent studies carried out by the LHC show significant deviation [7–9] that clearly indicates

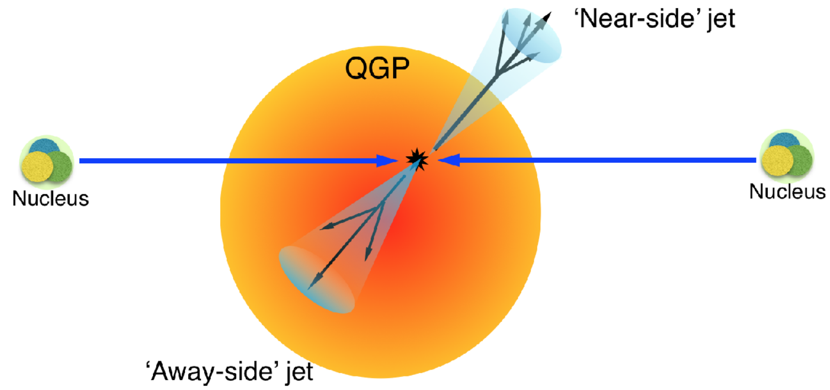

Figure 1–1: The schematic diagram for jet pair production. An 'near-side' jet and an 'away-side' jet are shown.

the influence of the medium on the yields of particles in the final state. Such measurements help us to gain important insights into how qualitative and quantitative analysis on the medium should be conducted.

Difficulties of studying jet quenching, however, lie in the limitations of probing the properties of the medium itself. This is in part due to a geometric bias toward a 'near-side' of the hard scatterings when measuring single hadron observables [10, 11]. The initial hard processes generate pairs of highly energetic partons traversing the medium in opposite directions and fragmenting into jets, i.e., di-jets. As shown in Fig. 1–1, the 'near-side' jet is closer to the surface of the QGP, while the 'away-side' jet moves in the opposite direction. Their losses of energy via interactions with the QCD medium are heavily dependent on the position and orientation of each vertex associated with the hard scattering. The 'near-side' jet of the di-jet pair is likely to survive during its propagation within the hot QCD medium, increasing trigger-bias.

On the other hand, the ‘away-side’ jet is absorbed in the medium as it is blocked by the relatively thicker medium and hence suffers a significant energy loss.

To resolve such difficulties, innovative techniques were newly introduced in RHIC and the LHC [12–15] for full jet reconstruction, which captures a whole bunch of particles in a pre-defined cone in order to restore the underlying partonic kinematics. This task requires to differentiate the hard scatterings that create the di-jet pair of interest from an ‘underlying event’ that always coincides with the foremost event. The underlying event (UE), by definition, contains all pieces of debris coming from heavy ion collisions which do not originate from the primary hard scattering process.

Though it is challenging to determine the soft background defined by the UE and its fluctuations, several algorithms [12, 16] were used to effectively reconstruct the ‘true’ jet momentum where the UE contribution is subtracted. The studies on the fully reconstructed jet enabled direct and unbiased estimations of the energies of primary parton in the initial state. With the help of the jet algorithms, the jet spectra in heavy ion collisions and the corresponding nuclear modification factors were measured in several detectors [17, 18]. These analyses facilitate comprehensive investigations of jet-medium dynamics and the jet suppression.

More recent ALICE results on p-Pb collisions indicate that the suppression of jet production is mainly induced by the QGP medium effects, not nuclear effects. The effects on the nuclear medium (e.g., a shadowing effect and initial-state energy loss) are dominant in p-Pb collisions, during which no medium is expected to form [19]. In the meantime, measurements of diet asymmetry, an imbalance of the reconstructed jet energies in opposite hemispheres, show a centrality dependency of the imbalance of leading and sub-leading jet momenta. A large broadening of the imbalance was observed among central collisions at the CMS and the ATLAS [20,21].

1.2 Objective and Organization

As can be seen in the previous section, understanding of the new phase of the QCD matter is the primary aim of heavy ion programs and ongoing tasks. It requires further developments of the experimental methodologies to probe the medium and extract valuable information from the measurements of such observables. On the other hand, constructing appropriate models based on the framework of our theoretical knowledge is another key element in the fulfillment of the ultimate goal.

Throughout this thesis I address the recent development of MARTINI, a Monte Carlo event generator for high-energy heavy ion collisions, along with the results of the nuclear modification factor, R_{AA}, and the di-jet asymmetry from Pb-Pb collisions at $\sqrt{s} = 2.76$TeV. The following is the outline of this thesis.

Chapter 2 will discuss the theoretical underpinning of the system in which the medium evolves, starting from the QCD Lagrangian. This will cover two phenomena occurring at opposite extreme limits: one is asymptotic freedom, where the energy scale is large and/or the distance scale is short, and the other is colour confinement, where the scale of the system is reversed. This will lead us to consider how they affect behaviours of the QGP in reality. The regime of heavy ion collisions will be mapped on a hadronic phase diagram. The finite temperature approach for radiative energy loss will be introduced. This Arnold-Moore-Yaffe formalism forms the foundation of the radiative energy loss rate in MARTINI and includes the Landau-Pomeranchuk-Migdal effect in $2 \leftrightarrow 2$ particle processes. It is summarized by constructing the effective kinetic theory based on the Boltzmann equation, including both $2 \leftrightarrow 2$ and $1 \leftrightarrow 2$ teams.

In Chapter 3, the basic ideas inherent in PYTHIA, the Monte Carlo event simulator, will be introduced. They will include the systematic flow of producing a collision event. The significant theoretical and phenomenological models supporting the validity of the each step in the flow will be described. Moreover, this chapter will discuss MARTINI, the essential means of studying the jet quenching in this thesis. The mechanism that creates collision events by PYTHIA and treats the partons coming from the collisions will be explained. To address the jet evolution scheme in MARTINI, the AMY formalism of the QCD version will be applied to the radiative energy loss rate, and the collisional processes will be also incorporated in the total jet energy loss rate. At the end, the effects of each process on the energy loss of a parton propagating in the medium will be shown, and the initial results from MARTINI compared to the RHIC data will be presented.

Chapter 4 will present two different models, which considering a formation time of emissions and running coupling, respectively. These models will be incorporated in MARTINI and improve the radiative processes in a realistic way. The Monte Carlo implementation scheme of MARTINI will be also described by following a full procedure of one heavy-ion event. This chapter will show the recent simulations of MARTINI using the new features. They include the charged hadron nuclear modification factor R_{AA} and dijet asymmetry A_J at different centrality classes compared with results from the CMS experiments. Finally, possibilities for further improvements of this study and models will be discussed.

In Conclusions, the models and the MARTINI results using the models will be briefly reviewed. Arguments for future works will be finally made.

CHAPTER 2
Theoretical Background

The theory of heavy ion collisions is an integration of highly sophisticated theoretical efforts. It serves as a sufficient means of verification of QCD, the underlying concept which plays an essential role in establishing the basis of dynamics of the strong interaction under extreme conditions. QCD, thus, enjoys the advantage of being an experimentally well studied theory, and understanding QCD provides us with a wealth of opportunities for constructing the theoretical foundation of heavy ion collisions.

We shall discuss, in Section 2.1, basic features of QCD and their applications, especially jet pair production and jet evolution in the weakly coupled QGP medium. Section 2.2 will address the Arnold-Moore-Yaffe approach to the radiative energy loss, which is implemented in MARTINI.

2.1 Quantum Chromodynamics

QCD is the theory of the strong interaction, one of the fundamental interactions of nature, between quarks and gluons. All species of baryons and mesons that can be observed are the bound states of quarks via the strong force. Since Gell-mann and Zweig independently proposed the quark models [22, 23], six flavours of quarks — up (u), down (d), strange (s), charm (c), top (t), and bottom (b) — have been discovered. These quarks have a new intrinsic quantum number, colour charge, and transform under the fundamental representation of the colour $SU(3)$ (in short $SU(3)_C$) symmetry groups. The strong interaction between quarks is mediated by gluons, massless spin-1 gauge bosons, analogous to the exchange of photons in the electromagnetic interaction.

The distinctive characteristics of QCD arises from the theoretical structure of a non-commuting local symmetry group. This results in the gluons themselves carrying the colour charge, contrary to photons in quantum electromagnetic (QED) which have no electric charge. Gluons have 8 combined colour states corresponding to 8 gauge fields of the adjoint representation of $SU(3)_C$, which, in turn, allows them to interact with quarks and themselves. The non-Abelian character of QCD is also responsible for the asymptotic freedom and colour confinement in QCD. To understand the way they are related to the non-abelian gauge theory, it is essential to address the Lagrangian of QCD and useful concepts in terms of a gauge theory.

2.1.1 QCD Lagrangian

Since $SU(3)_C$ is a non-abelian gauge group, QCD is the theory constructed on the basis of the $SU(3)$ Yang-Mills theory of quarks in fundamental representation, interacting with gluons in the adjoint representation. The Yang-Mills Lagrangian for QCD has the form

$$\mathcal{L}_{QCD} = \mathcal{L}_q + \mathcal{L}_g = \bar{\psi}(i\not{D} - m_q)\psi - \frac{1}{4}F_{\mu\nu}F^{\mu\nu}. \tag{2.1}$$

Note that the first term represents the quark Lagrangian describing the interaction of quark fields ψ, a 4-component Dirac-spinor, mediated by gluon fields. The covariant derivative D_μ plays an important role in local gauge invariance of the QCD Lagrangian and it is defined as

$$D_\mu = \partial_\mu - igA_\mu, \tag{2.2}$$

with

$$A_\mu = A_\mu^a \lambda_a, \tag{2.3}$$

where A_μ^a $(a = 1, 2, \cdots, 8)$ represents the 8 gauge fields corresponding to the 8 different gluons and λ_a the generator of $SU(3)$, called the Gell-mann matrices. Note that the generators are the Lie algebra:

$$[\lambda_a, \lambda_b] = if_{abc}\lambda_c, \tag{2.4}$$

where f_{abc} are the $SU(3)$ structure constants.

Although the structure of the QCD Lagrangian is analogous to that of the QED, the non-commuting vector field A_μ for gluons imposes a new term in the field strength tensor, $G_{\mu\nu}$, defined in terms of the commutator of the covariant derivative D_μ:

$$\begin{aligned} [D_\mu, D_\nu] &= -ig(\partial_\mu A_\nu^a - \partial_\nu A_\mu^a + gf_{abc}A_\mu^b A_\nu^c)\lambda_a \\ &= -igG_{\mu\nu}^a \lambda_a, \end{aligned} \tag{2.5}$$

with the definition of $G_{\mu\nu}^a$,

$$G_{\mu\nu}^a \equiv \partial_\mu A_\nu^a - \partial_\nu A_\mu^a + gf_{abc}A_\mu^b A_\nu^c. \tag{2.6}$$

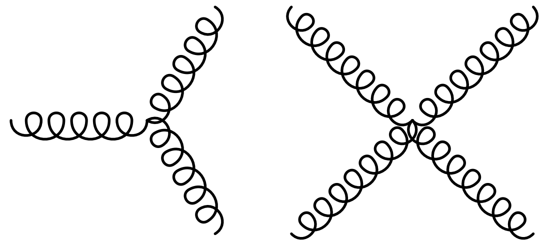

Figure 2–1: Feynman diagrams for gluon self-interactions

Equivalently,

$$G_{\mu\nu} \equiv G^a_{\mu\nu}\lambda_a = \frac{i}{g}[D_\mu, D_\nu]. \tag{2.7}$$

Therefore, besides the $\frac{1}{4}(\partial_\mu A_\nu - \partial_\nu A_\mu)^2$ term in the QED Lagrangian, the gluonic Lagrangian contains two additional terms due to the commutator of the covariant derivatives, which results in the possibility of gluons interacting by themselves. The Feynman diagrams for three- and four-gluon self interaction are shown in Fig. 2–1. Such distinct characteristics of the QCD Lagrangian are the main cause of the non-trivial dynamics of quarks and gluons that differentiate QCD from other field theories.

2.1.2 Asymptotic Freedom

One of the unique features of QCD is the asymptotic freedom. It states that the running coupling constant $\alpha_s(\mu^2)$ — the interaction strength that depends on the scale at which the measurement is performed — decreases at large energy scale μ or short distance r as roughly $\mu \sim 1/r$. This scale dependency is determined by the renormalization group, especially through the beta function $\beta(\alpha_s)$, and the theory predicts that [24]

$$\mu^2 \frac{\partial \alpha_s(\mu^2)}{\partial \mu^2} = \beta(\alpha_s(\mu^2)) = -\beta_0 \alpha_s^2(\mu^2) + \mathcal{O}(\alpha_s^3), \tag{2.8}$$

where

$$\beta_0 = \frac{33 - 2N_f}{12\pi} \tag{2.9}$$

is independent of the renormalization scheme, and N_f is the number of flavours. If we introduce a dimensionful parameter $\Lambda^2_{\rm QCD}$,

$$\Lambda^2_{\rm QCD} = \frac{Q^2}{e^{1/(\beta_0 \alpha_s(Q^2))}}, \tag{2.10}$$

with the choice of the reference scale as the mass of the Z^0 boson, $Q = M_{Z^0} =$ 91.2GeV, the solution for the beta function can be written as

$$\alpha_s(\mu^2) = \frac{1}{\beta_0 \ln(\mu^2/\Lambda^2_{QCD})}. \tag{2.11}$$

A recent study by the CMS reported that the strong coupling constant at M_{Z^0} is 0.1185 ± 0.0019 [25].

Since QCD has 6 flavours guarantees that the β_0 in Eq. (2.8) is always positive, the QCD coupling $\alpha_s(\mu^2)$ asymptotically approaches zero as the energy scale μ^2 diverges to infinity. Note that the first term in β_0 has contributions from the additional one-loop diagram in which the gluon self-interactions are involved, while these diagrams are absent in QED.

2.1.3 Quark Gluon Plasma

The ultraviolet behaviour of QCD, i.e., asymptotic freedom, predicted a new state of QCD matter freed from the restrictions of the strong interaction [31, 32]. At very high temperatures, $T \gg \Lambda_{QCD}$, where the coupling strength sufficiently diminishes, quarks and gluons are no longer confined to bound states. The QGP is the plasma-like state in which colourless hadrons are dissociated into quarks and gluons retaining their own colour degrees of freedom .

Another property of an intrinsic symmetry in QCD predicts the formation of the QGP as well. At low temperatures, the chiral symmetry of the QCD Lagrangian for massless quarks is spontaneously broken. This broken symmetry generates a discrete mass spectrum consisting of known hadrons, such as a pion and a proton. The spontaneously broken chiral symmetry, however, is restored at high temperatures, which guarantees the continuous spectrum of hadronic masses. The existence of the phase transition from the regime of ordinary hadronic matter to that governed by the deconfinement is manifested by the restoration of the broken chiral symmetry at a critical temperature T_c. The critical point may vary depending on the determination schemes, but the lattice QCD calculation shows that the critical temperature at baryon chemical potential μ_B, would be $T_c = 173 \pm 15$MeV [33].

Phase diagram

The illustration for the hadronic matter phase transition as a function of temperature and baryon chemical potential is shown in Fig. 2–2. As can ben seen in the figure, the QGP exists, under the conditions at which temperature and/or density

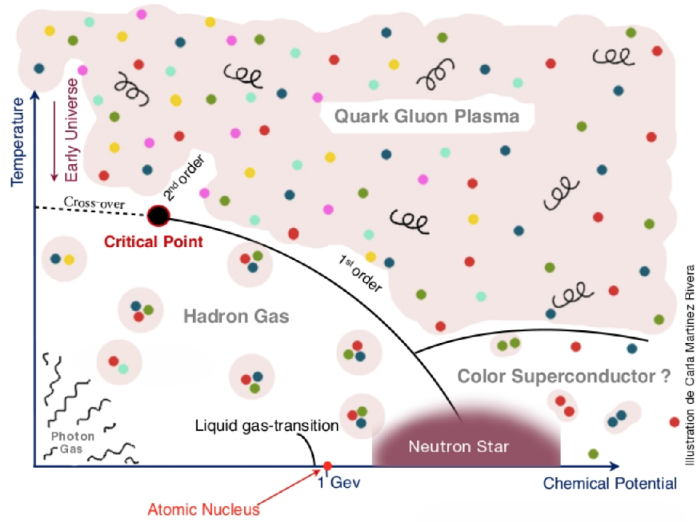

Figure 2–2: A schematic phase diagram for hadronic matter [34].

is extremely high. The top left corner of the diagram is of interest as it shows how contemporary heavy ion programs reach the exotic regime where the early universe is believed to start.

2.2 Arnold-Moore-Yaffe Formalism

The aim of this thesis is to study propagation of high-energy partons through the QGP. Quantum field theory at finite (or high) temperature investigates particles at equilibrium and provides a means of describing the medium created in heavy-ion collisions. Arnold, Moore and Yaffe (AMY) [35–38] proposed a formalism for the hard parton energy loss based on the thermal effective field theory. The AMY formalism describes energy loss of hard jets in heavy ion collisions as parton bremsstrahlung in the evolving QGP medium. In this approach, the QGP medium is thought to be fully equilibrated at asymptotically high temperature where the coupling constant is small $g \ll 1$. The effective kinetic theory described in [38] states that quarks and gluons in the medium are well-defined (hard) quasiparticles and they are assumed to have typical momentum of order T and thermal mass of order gT.

To describe the transport of the quasiparticles with sufficient precision, a set of Boltzmann equations are formulated, which is of the form [38],

$$(\partial_t + \boldsymbol{v} \cdot \boldsymbol{\nabla}_x) f(\boldsymbol{x}, \boldsymbol{p}, t) = -C[f], \tag{2.12}$$

where $f(\boldsymbol{x}, \boldsymbol{p}, t)$ is the phase space density of the particles and $C[f]$ represents the effect of collisions between the particles.

2.2.1 Collision Processes

The collision term $C[f]$ in Eq. (2.12) consists of two parts; $2 \leftrightarrow 2$ particle processes and collinear processes. The collinear processes are formally of a higher order in g. However, due to the collinear singularity, it contributes at the leading order. One can consider, as the formal case, ordinary Coulomb scatterings. The hard partons traversing the medium are nearly on-shell, experiencing soft scatterings with momentum transfer $q \equiv |\mathbf{q}| \sim gT$ [38]. Such soft scatterings have small opening angles $\theta \sim g$. One can parametrically estimate the mean free path of the process using the differential scattering rate [38],

$$\begin{aligned} d\Gamma &\sim g^4 T^3 \frac{dq}{q^3} \sim g^4 T^3 \frac{g dT}{(gT)^3} \\ &\sim g^2 dT, \end{aligned} \tag{2.13}$$

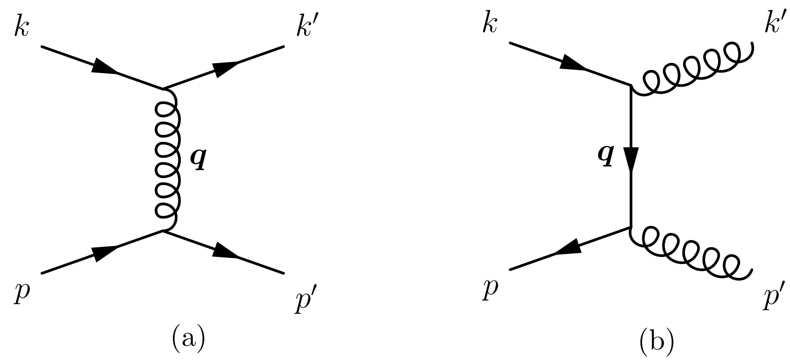

Figure 2–3: $2 \leftrightarrow 2$ particle processes by t-channel (a) gauge boson exchange, (b) $q\bar{q}$ annihilation.

which gives,

$$\tau \sim \Gamma^{-1} \sim (g^2 T)^{-1}. \tag{2.14}$$

It is also important to include a process where the type of an excitation is changed. For example, a quark-antiquark pair of momentum p can be converted into a pair of gluons by the soft $q\bar{q} \leftrightarrow gg$ process. The typical example of $2 \leftrightarrow 2$ particle processes are shown in Fig. 2–3.

In the meanwhile, the momentum exchange due to the soft scattering in the thermal medium induces an $1 \rightarrow 2$ splitting in which a hard quasiparticle splits into two collinear particles. Such near-collinear processes are kinematically allowed in the thermal medium. One example of the processes is a gluon bremsstrahlung following a soft gluon exchange between hard quasiparticle as depicted in Fig. 2–4. The mean free path for the $1 \rightarrow 2$ process can also be estimated as done for the soft process and is of order of $(g^4 T)^{-1}$, which is much larger than that for the soft scattering since $g \ll 1$ at high temperature. Detailed information of the analogous case of the QED

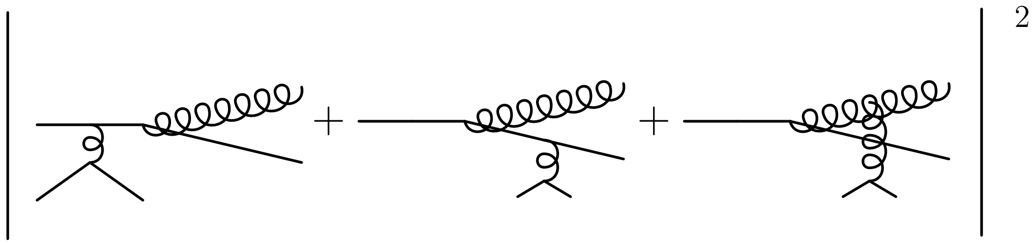

Figure 2–4: Leading order diagrams for the nearly collinear bremsstrahlung induced by a soft scattering in the thermal medium.

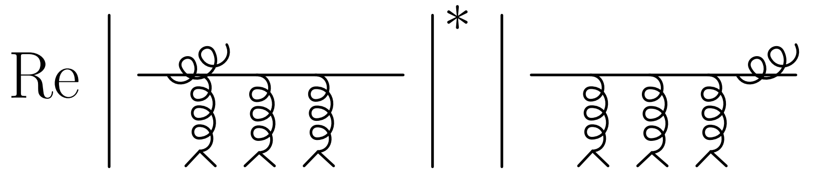

Figure 2–5: A diagram for $1 \to 2$ processes in which interferences between splittings before and after multiple soft scatterings occur. Many diagrams of this type contribute to the leading order splitting rate.

process can be found in Ref. [36].

2.2.2 LPM Effect

One should notice that the duration for the splitting process is not instantaneous; this process has a finite size of a formation time $t_f \sim (g^2T)^{-1}$, which can be estimated by

$$
\begin{aligned}
t_f &\sim \frac{l_\perp}{|\boldsymbol{v}_\perp|} \sim \frac{(1/gT)}{g} \\
&\sim \frac{1}{g^2T},
\end{aligned}
\tag{2.15}
$$

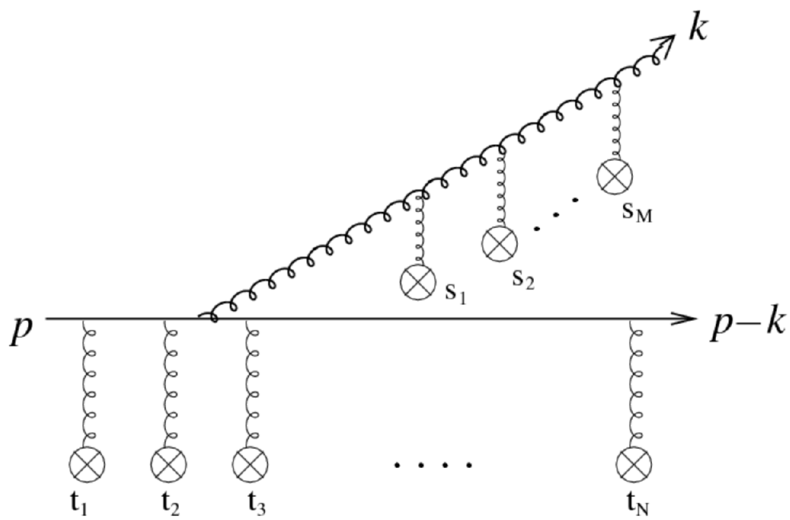

Figure 2–6: An example of a bremsstrahlung diagram to be summed in the AMY calculation.

where $l_\perp$ is the transverse size of a parton and $\boldsymbol{v}_\perp$ the transverse velocity of the emitted parton. This is of the same order of magnitude as the mean free path of the soft scattering. If the momentum of a hard parton is high enough, the formation time exceeds the mean free path for the soft exchange process due to the small momentum transfer q in the process. As a result, it is possible that multiple soft scattering occur within the formation time of the collinear process. This is where the Landau-Pomeranchuk-Migdal (LPM) effect arises.

Splittings induced by consecutive soft scatterings may not be treated as independent events due to the interference between them. It is, therefore, essential to consider interferences, as shown in Fig. 2–5. This interference term contributes to hard gluon bremsstrahlung at leading order in the coupling g. The bremsstrahlung rate in the thermal medium turned out to be sensitive to the processes in which the multiple soft scatterings are involved. In the original AMY formalism, however, no interference between vacuum and the medium radiation is included. In addition to that, $2 \to 1$ processes, where two hard particles collide each other and merge into a single particle, are also physically allowed in the medium and should be taken into account. The complete evaluation of $1 \leftrightarrow 2$ collinear processes, including $2 \to 1$ processes, can also be found in Ref. [37].

One can consider a situation where a hard quark undergoes gluon bremsstrahlung and all the hard partons recurrently interact with soft background medium at certain times t_i and s_i, as shown in Fig. 2–6. It is necessary to sum such diagrams and square the summation to calculate the leading order gluon emission rate in which the LPM effect is taken account. This task can be accomplished by evaluating the imaginary part of an infinite number of gluon self-energy diagrams. A generalized gluon ladder diagram is shown in Fig. 2–7. Fortunately, the contribution of this gluon ladder diagrams can be expressed in terms of a Schwinger-Dyson type equation, diagrams for which is illustrated in Fig. 2–8. The following corresponds to the integral equation for AMY formalism [39, 40],

$$
\begin{aligned}
2\mathbf{h} =& i\delta E(\mathbf{h}, p, k)\mathbf{F}(\mathbf{h}) + g_s^2 \int \frac{d^2\mathbf{q}_\perp}{(2\pi)^2} C(\mathbf{q}_\perp) \Big\{ (C_s - C_A/2)[\mathbf{F}(\mathbf{h}) - \mathbf{F}(\mathbf{h} - k\mathbf{q}_\perp)] \\
&+ (C_A/2)[\mathbf{F}(\mathbf{h}) - \mathbf{F}(\mathbf{h} + P\mathbf{q}_\perp) + (C_s - C_A/2)[\mathbf{F}(\mathbf{h}) - \mathbf{F}(\mathbf{h} - (p-k)\mathbf{q}_\perp)] \Big\}.
\end{aligned}
\tag{2.16}
$$

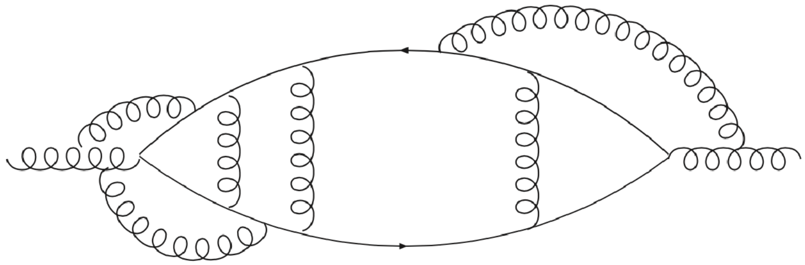

Figure 2–7: An example of Gluon Self-energy which is resumed in the AMY formalism [39].

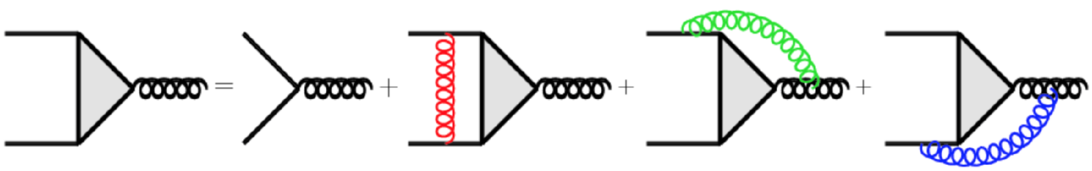

Figure 2–8: Diagrammatic illustration of the Schwinger-Dyson type equation for the emission vertex [41].

$C(\mathbf{q}_\perp)$ is the differential rate to exchange transverse momentum $\mathbf{q}_\perp$. In the QCD medium, the value at leading order in the strong coupling is given by [42]

$$C(\mathbf{q}_\perp) = \frac{m_D^2}{\mathbf{q}_\perp^2(\mathbf{q}_\perp^2 + m_D^2)}, \quad m_D^2 = \frac{g_s^2 T^2}{6}(2N_c + N_f). \tag{2.17}$$

Finally, $\delta E(\mathbf{h}, p, k)$ is the energy difference between the initial and final states [40]:

$$\delta E(\mathbf{h}, p, k) = \frac{\mathbf{h}^2}{2pk(p-k)} + \frac{m_k^2}{2k} + \frac{m_{p-k}^2}{2(p-k)} - \frac{m_p^2}{2p}, \tag{2.18}$$

where m_k^2 is the medium induced thermal mass of a parton carrying the momentum k.

2.2.3 Effective Kinetic Theory

Having realized the importance of the two relevant particle processes mentioned above, one can construct an effective kinetic theory. The Boltzmann equation in Eq. (2.12) becomes [38]

$$(\partial_t + \boldsymbol{v}\cdot\boldsymbol{\nabla}_x) f_s(\boldsymbol{x},\boldsymbol{p},t) = -C_s^{2\leftrightarrow 2}[f] - C_s^{1\to 2}[f], \tag{2.19}$$

where s indicates the partons to be excited in the medium and $C_s^{2\leftrightarrow 2}[f]$ and $C_s^{1\to 2}[f]$ correspond to the soft exchange and the nearly collinear processes, respectively.

The $2 \leftrightarrow 2$ soft scattering term can be expressed as [38]

$$\begin{aligned} C_a^{2\leftrightarrow 2}[f] =& \frac{1}{4|\boldsymbol{p}|\nu_a}\sum_{bcd}\int_{\boldsymbol{k}\boldsymbol{p}'\boldsymbol{k}'} \left|\mathcal{M}^{ab}_{cd}(\boldsymbol{p},\boldsymbol{k};\boldsymbol{p}',\boldsymbol{k}')\right|^2 (2\pi)^4\delta^{(4)}(P+K-P'-K') \\ &\times\Big\{ f_a(\boldsymbol{p})f_b(\boldsymbol{k})[1\pm f_c(\boldsymbol{p}')][1\pm f_d(\boldsymbol{k}')] - f_c(\boldsymbol{p}')f_d(\boldsymbol{k}')[1\pm f_c(\boldsymbol{p})][1\pm f_d(\boldsymbol{k})]\Big\}, \end{aligned} \tag{2.20}$$

where $a-d$ denote 4 independent species of participants in the collision, and ν_a the number of colour states multiplied by that of spin for a given species a. A short-hand notation for the Lorentz invariant momentum integration for massless particles is used in the equation,

$$\int_{\boldsymbol{p}} = \int \frac{d^3\boldsymbol{p}}{2|\boldsymbol{p}|(2\pi)^3}. \tag{2.21}$$

$\mathcal{M}^{ab}_{cd}$ represents an effective scattering magnitude for the process $ab \leftrightarrow cd$, and $|\mathcal{M}^{ab}_{cd}|^2$ reads the square of the matrix element summed over the spins and colours of the four particles. The distribution functions f_a is either Fermi-dirac or Bose-einstein distribution depending on the species of the parton a. The $+$ and $-$ signs represent Bose enhancement or Pauli blocking, respectively.

Similarly, $1 \leftrightarrow 2$ collinear bremsstrahlung term has the following form [38]

$$
\begin{aligned}
C_a^{1\leftrightarrow 2}[f] =& \frac{1}{4|\boldsymbol{p}|\nu_a} \sum_{bc} \int_{\boldsymbol{p'k'}} \left|\mathcal{M}^a_{bc}(\boldsymbol{p};\boldsymbol{p'},\boldsymbol{k'})\right|^2 (2\pi)^4 \delta^{(4)}(P - P' - K') \\
& \times \Big\{ f_a(\boldsymbol{p})[1 \pm f_b(\boldsymbol{p'})][1 \pm f_c(\boldsymbol{k'})] - f_b(\boldsymbol{p'}) f_c(\boldsymbol{k'})[1 \pm f_a(\boldsymbol{p})] \Big\} \\
& + \frac{1}{2|\boldsymbol{p}|\nu_a} \sum_{bc} \int_{\boldsymbol{kp'}} \left|\mathcal{M}^c_{ab}(\boldsymbol{p'};\boldsymbol{p},\boldsymbol{k})\right|^2 (2\pi)^4 \delta^{(4)}(P + K - P') \\
& \times \Big\{ f_a(\boldsymbol{p}) f_b(\boldsymbol{k})[1 \pm f_c(\boldsymbol{p'})] - f_c(\boldsymbol{p'})[1 \pm f_a(\boldsymbol{p})][1 \pm f_b(\boldsymbol{k})] \Big\},
\end{aligned}
\tag{2.22}
$$

where $|\mathcal{M}^a_{bc}|^2$ is same as in Eq. 2.20 but for the process $a \leftrightarrow bc$. From Eq. (2.22), the splitting rates for the processes such as $q \to qg$, $q \to gg$, and $g \to gg$ were calculated in [37]. These results are referred to as "AMY Formalism" in the later works [39, 43, 44].

2.2.4 Radiative energy loss

We discussed the LPM effect that needs to be included in the AMY formalism above. This is mainly due to the formation time of a radiative process τ_f having the same order of magnitude as the mean free time of a soft scattering τ_*. At asymptotically high temperature, both the BH (Bethe Heitler) limit ($\tau_f < \tau_*$) — the individual scattering limit — and the LPM limit ($\tau_f > \tau_*$) are well described by the solutions of the integral equation [37].

Given the process shown in Fig. 2–6, we can write down the gluon emission rate $d\Gamma(p,k)/dk$ in the QCD medium for various cases [39,40], which is closely related to the matrix elements $\left|\mathcal{M}^a_{bc}(\boldsymbol{p};\boldsymbol{p'},\boldsymbol{k'})\right|^2$ in Eq. (2.22).

$$\begin{aligned}\frac{d\Gamma(p,k)}{dk} =& \frac{C_s g_s^2}{16\pi p^7}\frac{1}{1\pm e^{-k/T}}\frac{1}{1\pm e^{-(p-k)/T}}\times\left\{\begin{array}{ll}\frac{1+(1-x)^2}{x^3(1-x)^2} & q\to qg\\ N_f\frac{x^2+(1-x)^2}{x^2(1-x)^2} & g\to qq\\ \frac{1+x^4+(1-x)^4}{x^3(1-x)^3} & g\to gg\end{array}\right\}\\ &\times\int\frac{d^2\mathbf{h}}{(2\pi)^2}2\mathbf{h}\cdot\mathrm{Re}\,\mathbf{F}(\mathbf{h},p,k),\end{aligned} \tag{2.23}$$

where C_s is the quadratic Casimir invariant, 4/3 for the processes involving quarks and 3 for the pure gluon processes, and g_s the strong coupling constant. $1/(1\pm e^{-k/T})$ is the Bose enhancement or Pauli blocking factor for the parton's final state after the transition ($-$ for gluons and $+$ for quarks). Here, $x \equiv k/p$ is defined as the momentum fraction of the radiated parton and N_f is the number of flavors. $\mathbf{h} \equiv (\mathbf{k}\times\mathbf{p})\times\mathbf{e}_{\parallel}$ determines how non-collinear the final state is, where $\mathbf{e}_{\parallel}$ is chosen by convention to a unit vector collinear with $\mathbf{p}$, $\mathbf{k}$ [37]. $\mathbf{F}(\mathbf{h},p,k)$ is the solution of the integral equation in Eq. (2.16).

CHAPTER 3
Monte Carlo Event Generator

In heavy ion physics, the experimental studies produce valuable information on the multiparton interactions in the QGP medium. A proper comparison of such experimental data and the theoretical expectation is necessary for physically meaningful interpretations of the data. Monte Carlo techniques allow us to simulate the heavy ion events as precisely as predicted by the theory and provides a way to compare theory with data.

Section 3.1 briefly introduces PYTHIA, widely used in high energy and heavy ion communities, and its procedure for simulating an entire course of nucleon-nucleon collisions. In Section 3.2, the basic concept of MARTINI and detailed formalisms for collisional and radiative processes of partons in the QGP medium are discussed. In addition, their effects on the energy loss of a jet as well as early MARTINI results with the default setting, compared to experimental data, are shown.

3.1 PYTHIA

PYTHIA [45, 46] is a popular, general-purpose event generator which generates either hadron-hadron or lepton-lepton collision events. Mostly, theories or phenomenological models on which PYTHIA is based are focused on high energy physics such as centre-of-mass energies $\sqrt{s} > 10$GeV for proton-proton collisions. At energies above the limit, certain parts of the program such as the pQCD (perturbative QCD) calculations of cross-sections and the fragmentation modelling are well-defined and yield reliable results. A user can select processes of interest (i.e., QCD process and Electroweak process) and simulating certain level of the event generation chain is possible as well. Free parameters in PYTHIA are required to be adjusted according to the collision system, most of which are closely associated with the area of non-perturbative QCD, such as multiparton interactions and hadronizations. PYTHIA provides several tunes, where the parameters are tuned based on certain parton distribution functions (PDFs) and experimental data.

3.1.1 Program flow

The main flow of the simulation in PYTHIA can be subdivided into three parts: initially, a process that decides the collision event of interest is created. At this level, all properties of incoming beams such as $\sqrt{s}$ and the nucleons are determined. The PDF selection is done according to the PYTHIA tune parameter or by linking the external LHAPDF package. The second stage controls the parton-level configuration after the primary scattering of the hard partons. The application of initial- and final-state radiation (ISR/FSR), multiparton interactions (MPI) and structures of beam remnants are involved in this stage. The last part of the simulation hadronizes jet partons with fragmentations and decays. Apart from the main procedures, PYTHIA also provide the interface for linking to external programs for special purposes. We shall discuss selected topics of important, regarding this thesis, among those mentioned above.

Parton Shower

The algorithms for ISR and FSR are based on $p_\perp$ ordered evolution [45]. Suppose a radiation process in which a mother parton a is split into a daughter b of energy fraction z and the remnant c having $1-z$ of the fraction. This process is formulated by a splitting kernel $P_{a\to bc}(z)$ which can be calculated in leading order QCD.

Initial state showers are space-like, whereas final state ones are time-like. Thus different treatments are required for the different sort of radiations, although separation between them are somewhat arbitrary. Differential branching probabilities for the ISR and FSR evolutions are, respectively [46],

$$\begin{aligned}\frac{d\mathcal{P}_{\rm ISR}}{dp_\perp^2} &= \frac{1}{p_\perp^2}\int_0^1 dz\frac{\alpha_s}{2\pi}P(z)\frac{f'(x/z,p_\perp^2)}{zf(x,p_\perp^2)},\\ \frac{d\mathcal{P}_{\rm FRS}}{dp_\perp^2} &= \frac{1}{p_\perp^2}\int_0^1 dz\frac{\alpha_s}{2\pi}P(z),\end{aligned} \tag{3.1}$$

where z is the energy-sharing fraction between daughter partons and $f(x,p_\perp^2)$ is the PDF of the radiating parton with momentum fraction x at energy scale $p_\perp^2$. The transverse-momentum variable in the shower evolutions is defined by [46]

$$p_\perp^2 = p_{\perp\rm evol}^2 = \begin{cases}(1-z)Q^2 & : \text{ISR}\\ z(1-z)Q^2 & : \text{FSR},\end{cases} \tag{3.2}$$

where, depending on the offshellness of the branching, $Q_{\rm ISR}^2 = (-p^2+m_0^2)$ and $Q_{\rm FSR}^2 = (p^2-m_0^2)$ so that $Q^2>0$. The leading order DGLAP splitting kernels, $P(z)$, shown in Eq. (3.1) are as follows [46]:

$$
\begin{aligned}
P_{q\to qg}(z) &= C_F \frac{1+z^2}{1-z}, \\
P_{q\to gq}(z) &= C_F \frac{1+(1-x)^2}{x} \\
P_{g\to gg}(z) &= C_A \frac{(1-z(1-z))^2}{z(1-z)}, \\
P_{g\to q\bar{q}}(z) &= T_R(z^2+(1-z)^2),
\end{aligned}
\tag{3.3}
$$

for QCD, where $C_F = 4/3$, $C_A = 3$, and $T_R = 1/2$. For QED,

$$
\begin{aligned}
P_{f\to f\gamma}(z) &= e_f^2 \frac{1+z^2}{1-z}, \\
P_{\gamma\to f\bar{f}}(z) &= e_f^2 N_C(z^2+(1-z)^2),
\end{aligned}
\tag{3.4}
$$

where $N_C = 1$ for charged leptons. These splitting kernels are used to evolve the PDF in Q^2.

Multiparton Interaction (MPI)

The multiparton cross section for perturbative QCD $2 \to 2$ scattering is given by [46]

$$
\frac{d\sigma_{2\to 2}}{dp_\perp^2} \propto \frac{\alpha_s^2(p_\perp^2)}{p_\perp^4} \to \frac{\alpha_s^2(p_\perp^2 + p_{\perp 0}^2)}{(p_\perp^2 + p_{\perp 0}^2)^2}. \tag{3.5}
$$

With the small shift by the parameter $p_{\perp 0}^2$, divergence of the multiparton cross section in the $p_\perp \to 0$ limit can be avoided. The integrated partonic cross section at the LHC energy scale exceeds that for the hadronic level. It is interpreted in the MPI model of PYTHIA such that several parton-parton collisions can be induced by single hadron-hadron collision, taking into account the fact that a hadron consists of several quarks and gluons. Besides $p_{\perp 0}^2$ that regulates the Infra-Red(IR) divergence, the value of MPI cross section is controlled by the value of $\alpha_s(M_z)$ and its running order, and the PDF set providing the parton luminosities for MPI.

Using the multiparton cross section in Eq. (3.5), one can roughly estimate the number of MPI per non-diffractive hadron-hadron collision for a given $p_{\perp 0}$:

$$\langle n_{\mathrm{MPI}}(p_{\perp 0})\rangle = \frac{\sigma_{2\to 2}(p_{\perp 0})}{\sigma_{\mathrm{ND}}}, \tag{3.6}$$

where the non-diffractive cross section σ_{ND} for a given energy scale s takes the form

$$\sigma_{\mathrm{ND}}^{\mathrm{pp}}(s) = \sigma_{\mathrm{INEL}}^{\mathrm{pp}}(s) - \int \left(d\sigma_{\mathrm{SD}}^{\mathrm{pp}\to\mathrm{Xp}}(s) + d\sigma_{\mathrm{SD}}^{\mathrm{pp}\to\mathrm{pX}}(s) + d\sigma_{\mathrm{DD}}^{\mathrm{pp}}(s) + d\sigma_{\mathrm{CD}}^{\mathrm{pp}}(s) \right). \tag{3.7}$$

In PYTHIA, the inelastic cross section σ_{INEL} is derived by

$$\sigma_{\mathrm{INEL}} = \sigma_{\mathrm{TOT}} - \sigma_{\mathrm{EL}}, \tag{3.8}$$

where σ_{TOT} is the total cross section and σ_{EL} the elastic cross section, and it can be divided into single-diffractive σ_{SD}, double-diffractive σ_{DD}, central-diffractive σ_{CD}, and non-diffractive σ_{ND} cross section.

With the help of the $p_\perp$ ordered evolution in which the hardest MPI is first generated, one can construct the probability for an parton-parton interaction, i, by a Sudakov-type equation [46],

$$\frac{d\mathcal{P}_{\mathrm{MPI}}}{dp_\perp} = \frac{1}{\sigma_{\mathrm{ND}}}\frac{d\sigma_{2\to 2}}{dp_\perp}\exp\left(-\int_{p_\perp}^{p_{\perp i-1}} \frac{1}{\sigma_{\mathrm{ND}}}\frac{d\sigma_{2\to 2}}{dp'_\perp}dp'_\perp \right), \tag{3.9}$$

where $p_{\perp i-1}$ is the $p_\perp$ scale of the previous step. As expected from a geometric picture of nucleon-nucleon collisions, the probability for MPI has the impact-parameter dependence. The large overlap area between two colliding proton yields the large number of the parton-parton interaction.

The expression for MPI in Eq. (3.9) can be integrated with ISR and FSR in Eq. (3.1) by applying the single common sequence of decreasing $p_\perp$,

$$\begin{aligned}\frac{d\mathcal{P}}{dp_\perp} = &\left(\frac{d\mathcal{P}_{\mathrm{MPI}}}{dp_\perp} + \sum \frac{d\mathcal{P}_{\mathrm{ISR}}}{dp_\perp} + \sum \frac{d\mathcal{P}_{\mathrm{FSR}}}{dp_\perp}\right) \\ &\times \exp\left(-\int_{p_\perp}^{p_{\perp i-1}} \left(\frac{d\mathcal{P}_{\mathrm{MPI}}}{dp'_\perp} + \sum \frac{d\mathcal{P}_{\mathrm{ISR}}}{dp'_\perp} + \sum \frac{d\mathcal{P}_{\mathrm{FSR}}}{dp'_\perp}\right) dp'_\perp\right). \end{aligned} \tag{3.10}$$

Fragmentation

As mentioned in previous chapter, at long distance, the pQCD calculation breaks down and colour confinement appears. Under this circumstance, the coloured quarks and gluons produced by collisions merge into colourless hadrons at the final state. However, the process of fragmentation is not fully understood in the theory of QCD. Instead, several phenomenological models exist to depict the process of fragmentation.

In PYTHIA, the fragmentations framework has been based on the Lund model [47, 48] from the beginning. This model uses hypothetical strings to connect different coloured partons so that their colours become neutral and both their energies and momenta are shared. The iterated operations of the connection are governed by a probabilistic rule. Moreover, the string described by the model has characteristics of a flux tube, which is supported by the lattice QCD prediction. One can imagine the simplest case, where $q\bar{q}$ pair is bounded by a string. As the $q\bar{q}$ pair moves apart, the potential energy stored in the string (tube) linearly increases and may break up, producing an additional $q\bar{q}$ pair. An initial parton where the connection of strings starts off in a given event is chosen arbitrary and any ordering of fragmentation processes should be equivalent.

3.2 MARTINI

MARTINI (Modular Algorithm for Relativistic Treatment of heavy IoN Interactions) is a Monte Carlo event generator developed by Shenke, Gale, and Jeon [49]. The main purpose is to simulate jets in heavy ion collisions and compare the results with the experimental data. The schematic diagram for MARTINI is illustrated in Fig. 3–1. Initially, PYTHIA 8.2 is used to generate nucleon-nucleon collisions and send information about the hard partons to MARTINI. Then it deals with the parton evolution in the QGP medium according to the AMY formalism for the radiative energy loss rates combined with the collisional processes, which is shown in the black dotted box in Fig. 3–1. Finally, hadronization (see Section 3.1) of the evolved partons is performed based on the Lund string model, which is provided by PYTHIA.

The background of thermal medium currently implemented in MARTINI is generated using MUSIC (MUScl for Ion Collisions) [50], a (3+1) dimensional hydrodynamics simulator. It uses the MUSCL (Monotonic Upstream-Centered Scheme for Conservation Laws) scheme which is also known as the Kurganov-Tadmor scheme. Any of soft medium calculations from several groups [40, 51–55] can be used in MARTINI, since the choice of the background evolution in MARTINI is flexible.

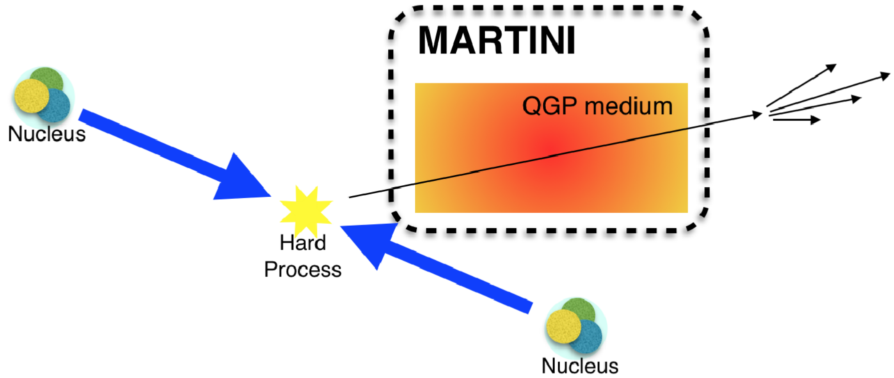

Figure 3–1: The schematic Diagram of MARTINI, which takes care of the medium evolution of hard partons generated by PYTHIA.

These backgrounds provides information on the temperature and flow velocity of the medium. In this study, we use (3+1) dimensional ideal hydrodynamics background in which jets are evolved.

3.2.1 Jet Evolution Scheme

The jet energy loss mechanism in MARTINI is based on the AMY formalism for radiative energy loss, combined with the collisional energy loss [43, 44]. The time evolution of the jet momentum distribution $P_a(p,t)$ for a given parton a in the medium is expressed in terms of a set of coupled rate equations, which takes the following form [40]:

$$
\begin{aligned}
\frac{dP_q(p)}{dt} = & \int_k P_q(p+k)\frac{d\Gamma^q_{qg}(p+k,p)}{dk} - P_q(p)\frac{d\Gamma^q_{gg}(p,k)}{dk} + \\
& + 2P_g(p+k)\frac{d\Gamma^g_{q\bar{q}}(p+k,k)}{dk}, \\
\frac{dP_g(p)}{dt} = & \int_k P_q(p+k)\frac{d\Gamma^q_{qg}(p+k,p)}{dk} + P_g(p+k)\frac{d\Gamma^g_{gg}(p+k,k)}{dk} \\
& - P_g(p)\left(\frac{d\Gamma^g_{q\bar{q}}(p,k)}{dk} + \frac{d\Gamma^g_{gg}(p,k)}{dk}\theta(2k-p)\right)
\end{aligned}
\tag{3.11}
$$

$d\Gamma^a_{bc}(p,k)/dk$ is the transition rate for a process where a parton a of energy p emits a parton c of energy k and becomes a parton b. In Eq. (3.11), $d\Gamma^g_{q\bar{q}}(p+k,k)/dk$ is identical to $d\Gamma^g_{q\bar{q}}(p+k,p)/dp$. The factor of 2 takes into account the fact that q and $\bar{q}$ are distinguishable. However, for the process $d\Gamma^g_{gg}(p+k,k)/dk$, the two gluons are identical, resulting in no additional factor. The θ function appears to avoid double-counting of final states. Note that the equation includes the integration where $k < 0$, representing the energy gain of the parton a.

Collisional energy loss

In MARTINI, the energy loss rate due to $2 \to 2$ scatterings at leading order in g, as shown in Fig. 3–2, is given by [44, 49]

$$
\begin{aligned}
\frac{d\Gamma_{\mathrm{el}}}{d\omega}(E,\omega,T) = d_k \int_{kk'} & \frac{2\pi}{4pp'}\delta(p-p'-\omega)\delta(k'-k-\omega) \\
& \times |\mathcal{M}|^2 f(k,T)(1 \pm f(k',T)),
\end{aligned}
\tag{3.12}
$$

where d_k is the degeneracy factor for the initial thermal partons and $\int_k = \int \frac{d^3k}{(2\pi)^3 2k}$ the Lorentz invariant momentum integral. $p = E = |\mathbf{p}|$ and $p' = |\mathbf{p}'|$ are, respectively, the absolute values of the momenta of the incoming and outgoing particles, and the same holds for $k = |\mathbf{k}|$ and $k' = |\mathbf{k}'|$. The two delta functions indicate the energy conservation relations for the transferred energy, $\omega = p - p' = k' - k$. The Fermi-Dirac or Bose-Einstein distribution f appears with the $+$ and $-$ signs corresponding to the Pauli blocking and Bose enhancement, respectively. $|\mathcal{M}|^2$ is the scattering matrix element squared at leading order and is dominated by the t-channel in the high-energy limit $E \gg T$. The elements for different processes are as follows [44].

$$
\begin{aligned}
|\mathcal{M}|^2_{qq} &= \frac{4}{9} g^4 \frac{s^2 + u^2}{t^2}, & |\mathcal{M}|^2_{qg} &= 2g^4 \left(1 - \frac{su}{t^2}\right), \\
|\mathcal{M}|^2_{gq} &= 2g^4 \left(1 - \frac{su}{t^2}\right), & |\mathcal{M}|^2_{gg} &= \frac{9}{2} g^4 \left(\frac{17}{8} - \frac{su}{t^2}\right),
\end{aligned}
\tag{3.13}
$$

where the subscripts in the matrix element denote two incoming particles. The Mandelstam variables are given by [44]

$$
\begin{aligned}
s &= -\frac{t}{2q^2} \Big[\{(p + p')(k + k') + q^2\} \\
&\qquad - \cos(\phi_{pq|kq}) \sqrt{(4pp' + t)(4kk' + t)} \Big], \\
t &= \omega^2 - q^2, \\
u &= -s - t.
\end{aligned}
\tag{3.14}
$$

$\phi_{pq|kq}$ is defined as the angle between the $\mathbf{p} \times \mathbf{q}$ and the $\mathbf{k} \times \mathbf{q}$ plane.

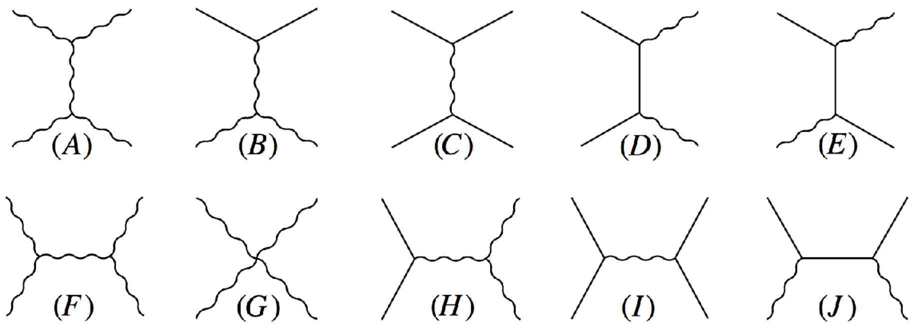

Figure 3–2: The diagrams for all possible leading order $2 \to 2$ scattering processes in a gauge theory. Fermions and gauge bosons are corresponding to solid lines and wiggly lines, respectively. Flow of time may be horizontal, in either way [38].

To deal with the transition rate shown in Eq. (3.12), one can replace $\mathbf{k}'$ integration by the exchanged momentum $\mathbf{q} = \mathbf{p} - \mathbf{p}' = \mathbf{k}' - \mathbf{k}$ and separate the contribution from soft $\sim gT$ and that from hard $\sim \sqrt{ET}$ momentum exchange as done in [56,57].

Eq. (3.12) can be rewritten in terms of the integration to q in the limit $p \to \infty$ [44]:

$$\frac{d\Gamma_{\rm el}}{d\omega}(E,\omega,T) = \frac{d_k}{(2\pi)^3}\frac{1}{16E^2}\int_0^p dq \int_{\frac{q-\omega}{2}}^{\infty} dk\theta(q-|\omega|) \times \int_0^{2\pi}\frac{d\phi_{kq|pq}}{2\pi}|\mathcal{M}|^2 f(k,T)(1\pm f(k',T)), \tag{3.15}$$

where it is assumed that $\mathbf{q}$ is on the z-axis and $\mathbf{p}$ in the x-z-plane. The θ function in Eq. (3.15) imposes the momentum restriction, $-q < \omega < q$. For calculating soft part of the integration, an effective thermal gluon propagator was used [44,56], for which expression is given by

$$D^{\mu\nu}(Q) = \delta^{\mu0}\delta^{\nu0}\Delta_L(\omega,q) + P_T^{\mu\nu}\Delta_T(\omega,q), \tag{3.16}$$

where the components of $P^{\mu\nu}$ are such that

$$P^{00} = 0,$$
$$P^{ij} = \delta^{ij} - \hat{q}^i \hat{q}^j, \tag{3.17}$$

and the longitudinal and transverse gluon propagators are, respectively,

$$\Delta_L(\omega, q) = \frac{-1}{q^2 - m_g^2 \left[x \ln\left(\frac{x+1}{x-1}\right) - 2 \right]},$$
$$\Delta_T(\omega, q) = \frac{-1}{q^2(x^2-1) - m_g^2 \left[x^2 + \frac{x}{2}(1-x^2) \ln\left(\frac{x+1}{x-1}\right) \right]}. \tag{3.18}$$

The angular integration with the matrix element for e.g., $qq \to qq$ scattering can be evaluated as [44]

$$\int \frac{d\phi_{kq|pq}}{2\pi} |\mathcal{M}|^2_{qq} = \frac{8}{9} g^4 p^2 \Bigg[\left\{ (k+k')^2 - q^2 \right\} |\Delta_L|^2 + \frac{1}{2}\left(1 - \frac{\omega^2}{q^2}\right)^2 \left\{ (k+k')^2 + q^2 \right\} |\Delta_T|^2 \Bigg]. \tag{3.19}$$

Eq. (3.19) can be simplified in the limit of small ω and q as followings [44]

$$\int \frac{d\phi_{kq|pq}}{2\pi} |\mathcal{M}|^2_{qq} = \frac{32}{9} g^4 p^2 k k' \times \left[|\Delta_L|^2 + \frac{1}{2}\left(1 - \frac{\omega^2}{q^2}\right)^2 |\Delta_T|^2 \right]. \tag{3.20}$$

The calculation is logarithmically divergent at the lower limit of integration and incorporates a plasma screening effect through hard thermal loop corrections for soft momenta. These procedure allows for a numerical calculation of Eq. (3.12). Finally the transition rate as a function of both the transferred energy and momentum $d\Gamma/d\omega dk$ is obtained by omitting the integration over k in Eq. (3.12). In MARTINI, it is used for sampling the transferred energy and momentum in an elastic process.

Conversion process

Not only the gluon radiation processes described above, MARTINI also includes the conversion between quarks and gluons $q \leftrightarrow g$, due to the Compton scatterings and annihilation (for example, Fig. 2–3), as well as a jet-photon conversion process $q \to \gamma$. These contributions come from the soft scatterings of jets with the medium, where momentum transfer q is small. Typical examples of the jet-photon conversion process are shown in Fig. 3–3. The transition rate for the jet-photon conversion, obtained by the calculation analogous to that of gluon radiation, is expressed as [49]

$$\frac{d\Gamma^{\rm conv}_{q\to\gamma}}{d\omega}(E,\omega) = \left(\frac{e_f}{e}\right)^2 \frac{2\pi\alpha_e\alpha_s T^2}{3E}\left(\frac{1}{2}\ln\frac{pT}{m_q^2} - 0.36149\right)\delta(\omega), \tag{3.21}$$

where e_f is the colour charge of a quark of flavor f and $\alpha_e = e^2/4\pi$ the fine structure constant. One has to deal with the IR divergence in the limit $m_q^2 \to 0$, and this can be regulated by replacing m_q^2 in by a thermal mass $m_{\rm th}^2 = g^2T^2/6$ [58, 59]. Here, the quark to be converted is assumed to have the energy E much higher than the background temperature T, $E \gg T$, and the energy loss during the process is neglected as implied in the δ function. The conversion rates between $q \leftrightarrow g$ have simply the identical expression to that of jet-photon process, multiplied by some factors such that [49]

$$\begin{aligned}\frac{d\Gamma^{\rm conv}_{q\to g}}{d\omega} &= C_F\frac{d\Gamma^{\rm conv}_{q\to\gamma}}{d\omega},\\ \frac{d\Gamma^{\rm conv}_{g\to q}}{d\omega} &= N_f\frac{N_c}{N_c^2-1}\frac{d\Gamma^{\rm conv}_{q\to\gamma}}{d\omega},\end{aligned} \tag{3.22}$$

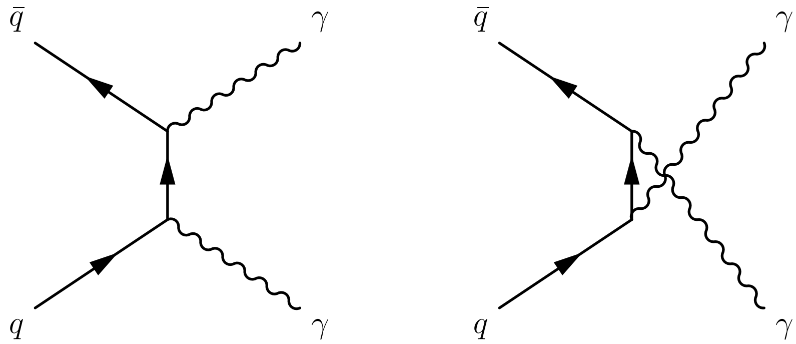

Figure 3–3: Leading order feyman diagrams for the jet-photon conversion processes.

where $C_F = 4/3$ is a colour factor.

3.2.2 Default results from MARTINI

This section shows early MARTINI results with the default setting prior to the improvements on the jet energy loss, which is discussed in the next chapter. Several works were carried out to test the validity of the collisional energy loss [44] described above and the performance ability of MARTINI with both radiative and collisional processes [49]. To examine the effect of collisional and radiative particle process on a time-dependent parton energy distribution spectrum, one may start from evaluating Eq. (3.11).

In Ref [44], the radiative energy loss rates obtained from different methods are examined. The first method (A) uses Eq. (3.12) and divides the integration range into two part as described above. In this calculation, Eq. (3.20) is directly inserted into Eq. (3.15). The two momentum regions of the contributions are matched at an intermediate value, $q^{*2} \sim \sqrt{ET}m_g$ [44]. On the other hand, the second method (B) applies Eq. (3.12) to the whole region of momentum integration. To achieve this

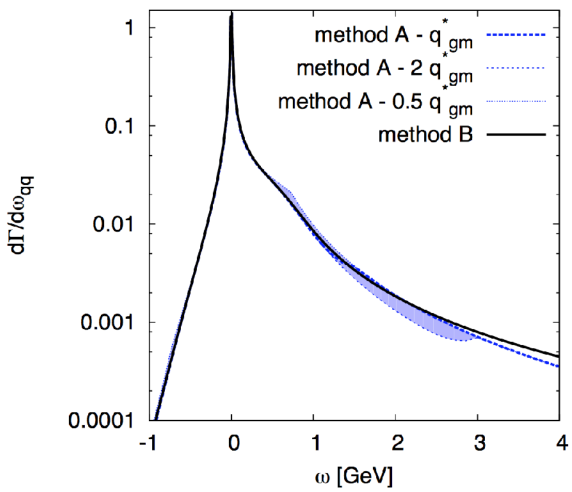

Figure 3–4: Comparison between the transition rates obtained from the two different methods. The process $qq \to qq$ at the initial energy of 10GeV and temperature of 200MeV is calculated in each method [44].

method, Eq. (3.19) is used to calculate the collisional energy loss rate numerically. In this approximation, additional momentum scale q is not required.

Lastly, the diffusion method for transition rates, used in [43], are presented and compared with the previous two methods. In this approach, the scattering process are approximated by introducing the drag term, $(dp/dt)dP(p)/dp$, and the diffusion term, $T(dp/dt)d^2P(p)/dp^2$, detailed information on which can be found in [60, 61].

Fig. 3–4 shows comparison between the transition rate obtained from the first (method A, blue lines) and the second method (method B, black solid line). For method A, the value of q^* is chosen to the geometric mean value q^*_{gm} and varied from $0.5q^*_{gm}$ to $2q^*_{gm}$. A good agreement between two methods can be seen at the low ω region. The small deviation results from the assumption that $-t \gg s$ and $s \sim -u$ [62, 63]. It can be neglected in the high-energy jet evolution since the

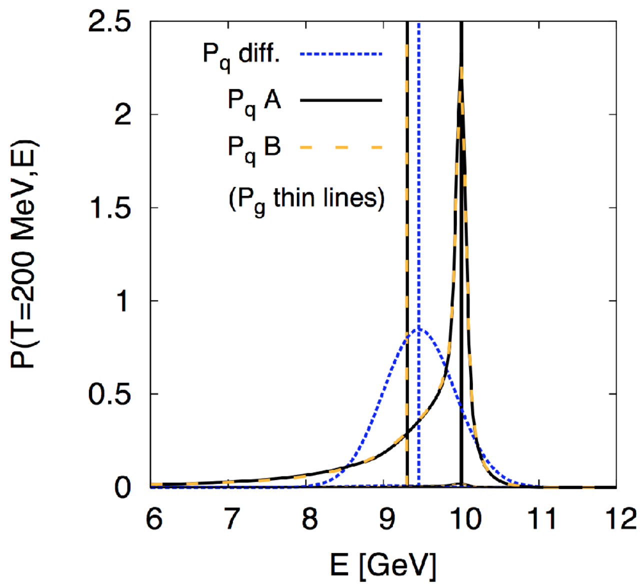

Figure 3–5: Comparison of the momentum distribution between the three different methods. A quark jet with the initial energy of 10GeV propagates through a static medium of temperature $T = 200\text{MeV}$ at $\alpha_s = 0.3$ for 2fm [44].

contribution from the elastic scattering increases logarithmically and the collisional energy loss is relatively dominant only in the regime where the energy transfer is small.

The momentum distributions obtained from the three different methods described above are compared in Fig. 3–5. A quark jet with the initial energy of 10GeV passes through a static medium of temperature $T = 200\text{MeV}$ and the momentum distributions are computed after 2fm of propagation time. In Fig. 3–5 the method A and B are depicted in the black solid and the orange dashed line, respectively, and the blue dotted line corresponds to the diffusion method. The vertical line at 10GeV represents the initial energy of the quark and those at below 10GeV indicates the mean energy of the quark after 2fm. One can notice that the method

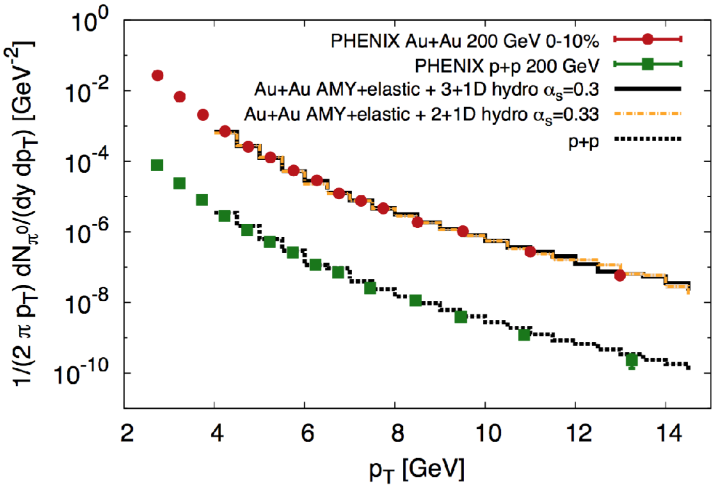

Figure 3–6: Neutral pion spectra in pp collisions and $0 - 10\%$ centrality AuAu collisions at RHIC energy. The different backgrounds are used for PbPb collisions [49].

A and B exhibit almost identical mean energy loss for elastic processes, while the diffusion method results in the significantly different amount of the mean energy loss from those from the method A and B. This difference between the diffusion method and the others occurs for the momentum distribution. The results computed by the method A and B show good agreement with each other, but an apparent discrepancy between they and that from the diffusion method is observed. Therefore, method B is used in the default MARTINI.

The capability for MARTINI to reproduce the heavy ion collisions at RHIC is also examined in Ref [49]. The spectrum of neutral pions π^0 in AuAu collisions as well as pp collisions at RHIC energy scale is presented in Fig. 3–6. A centrality of AuAu collisions is $0 - 10\%$ and PHENIX data [64] are compared with the results. The centrality class of a given event is determined by how much the two nucleus overlap when they collides, e.g., 10% most central events are the 10% those having

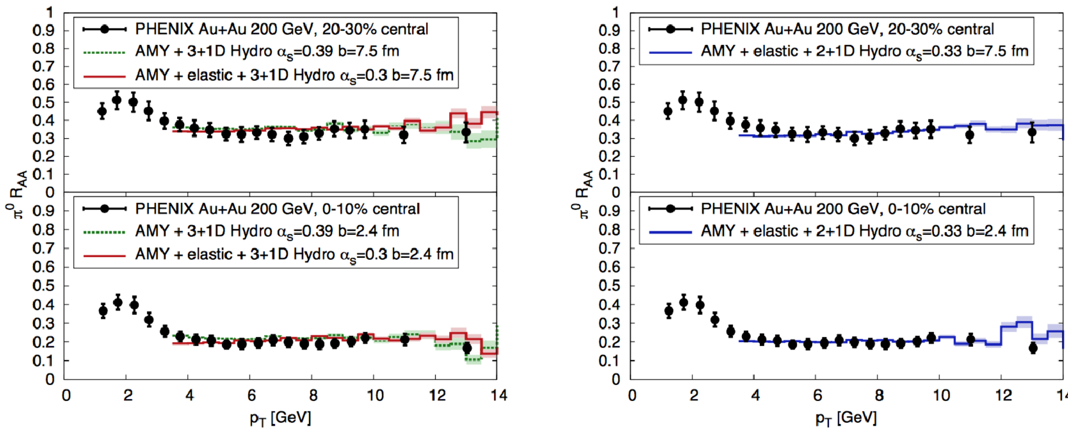

Figure 3–7: Nuclear modification factor R_{AA} for neutral pions in central and mid-central rapidities compared to the PHENIX data [49].

the highest number of participants. The simulations adopted CTEQ5L parton distribution functions [65], which include nuclear shadowing effects using the EKS98 parametrization [66]. For Au-Au collisions, $(3+1)$ dimensional hydrodynamics [54] and $(2+1)$ dimensional hydrodynamics [52,53,67] were used to describe the medium, which correspond to the black solid line and the orange dashed-dot line, respectively. The couplings α_s of 0.3 for (3+1) D and 0.33 for (2+1) D are selected to fit the neutral pion nuclear modification factor R_{AA} in most central collisions at PHENIX, shown below. The black dot represents pp collisions. With both collisional and radiative energy loss rates, MARTINI results of pp and AuAu spectra show good agreement with the experimental data.

The spectra of the final hadrons can be directly used to calculate the nuclear modification factor R_{AA}, which is defined by

$$R_{AA} = \frac{1}{N_{\text{coll}}(b)} \frac{dN_{AA}(b)/d^2p_T dy}{dN_{pp}/d^2p_T dy}, \tag{3.23}$$

where AA indicates the nuclei A colliding each other and b the impact parameter. In Fig. 3–7, the results of neutral pion R_{AA} in AuAu collisions at $\sqrt{s} = 200$GeV are presented. The collisions were made in two different centrality classes: $0-10\%$ (lower panel) and $20-30\%$ (upper panel), corresponding to the mean impact parameters of 2.4fm and 7.5fm, respectively. The left figure shows the results using the $(3+1)$ dimensional hydrodynamic background, while in the right one, the medium was described by $(2+1)$ dimensional hydrodynamics. The coupling constants are same as in the calculation in Fig. 3–6. It is found that the results in all centrality classes and all background medium nicely describe the PHENIX data.

CHAPTER 4
New effects in the radiative energy loss

The phenomenon of jet quenching has become an essential subject to explore the QCD medium created by heavy ion collisions. For better interpretations of experimental results and better understanding of the medium, we need to to develop MC event generators equipped with theoretically sound models and well reproducing observables under various environments. As introduced in Chapter 3, MARTINI is one of the Monte Carlo (MC) event generators for simulating jets in heavy ion collisions. We discussed the performance of MARTINI on the jet evolution in hydrodynamics medium and found that MARTINI faithfully reproduces final state observables such as momentum distributions and nuclear modification factor R_{AA} at the low p_T region $\sim$ 15GeV. However, as can be seen in Fig. 4–1 [3], theoretical models and event generators [68–73] have predicted gradually rising R_{AA} at extended energy scale. This argument was supported by experimental measurements made by various detectors [74–78] at different kinematical ranges. For example, the CMS data, plotted in the black dots in Fig. 4–1, shows that jet quenching at $p_T \sim$ 100GeV is notably reduced compared to that at $p_T \sim$ 10GeV. Considering the monotonic R_{AA} curves obtained from MARTINI (see Fig. 3–7), it is required to improve jet energy loss mechanisms that account for such high p_T phenomena. This also leave possibilities for MARTINI to be upgraded for better performances. We shell discuss the newly improved version of MARTINI as well as its results of jet quenching observables.

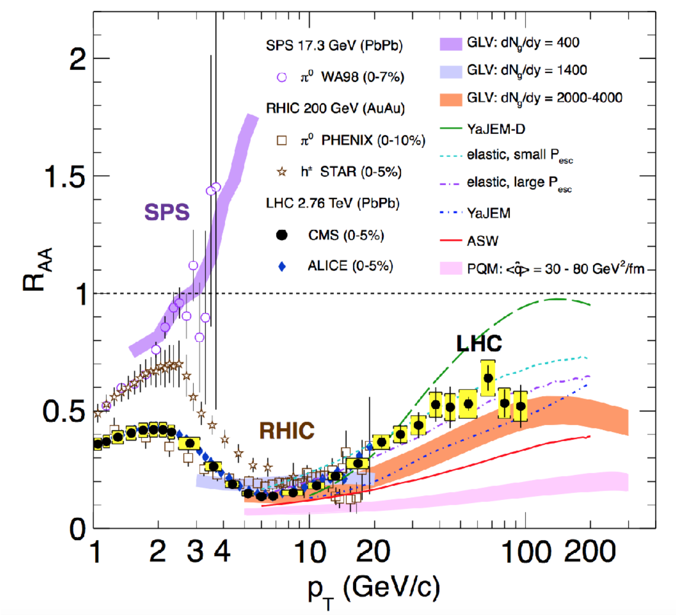

Figure 4–1: Experimental measurements of nuclear modification factor R_{AA} for heavy ion collisions from various detectors [74–78], compared to several theoretical predictions [68–73]. This figure is taken from [3].

In Section 4.1, two effects which are recently included in MARTINI and their results are presented. How the radiative energy loss rate has altered by the models is described. Section 4.2 explains strategies for the Monte Carlo implementation to simulate heavy ion collisions using MARTINI. It covers the way MARTINI simulates nucleus-nucleus collisions using PYTHIA and deals with hard partons and their evolutions in the medium. Not only that, the hydrodynamical backgrounds used in this study are also described. Section 4.3 presents the MARTINI results of two observables of important: the leading hadron R_{AA} and dijet asymmetry compared to experimental data. Finally, limitations on this study and possible further improvements are addressed in Section 4.4.

4.1 Models

This section introduces the two individual works prior to this study: a finite-size effect [1] and running coupling [2]. The new features in MARTINI are modelled based on these works. The former study modified the radiative energy loss of partons in the QGP medium by applying the finite size effect to the radiative processes. This suppresses the radiation rate at early times of partons' propagation. The latter investigated the effect of the running coupling on the radiative processes and showed the MARTINI results of the leading hadron R_{AA}. The followings are the detailed descriptions of the studies and how we modelled them.

4.1.1 Finite-size Effect

The study carried by C. Simon and C. Gale [1] shows the finite-size effect on the radiative energy loss of hard partons evolving in the QGP medium. The calculation starts by invoking the light-cone path integral formalism derived by Zakharov [79,80],

$$\frac{dP^a_{bc}}{dk} = \frac{P^{a(0)}_{bc}(x)}{\pi p} \times \mathrm{Re}\int_0^\infty dt_1 \int_{t_1}^\infty dt_2 \frac{\partial}{\partial \mathbf{x}}\frac{\partial}{\partial \mathbf{y}}[K(t_2, \mathbf{x}; t_1, \mathbf{y}) - (\mathrm{vac})]_{\mathrm{x=y=0}}, \qquad (4.1)$$

representing the total probability for a parton a of energy p, created at time $t = 0$ being split into partons b and c with energies of k, $p - k$, respectively. $P^{a(0)}_{bc}(x)$ represent DGLAP splitting kernels [81–85] for a given process $a \to bc$ with the longitudinal momentum fraction of the particle b with $x = k/p$. The splitting kernels are

$$P_{bc}^{a(0)}(x) = \begin{cases} g^2 C_F \frac{1+(1-x)^2}{x}, & g \to gq \\ g^2 C_A \frac{1+x^2+(1-x)^4}{x(1-x)}, & g \to gg \\ 2g^2 N_F T_F [x^2 + (1-x)^2], & g \to q\bar{q} \\ e^2 \frac{1+(1-x)^2}{x}, & e \to \gamma e \end{cases} \tag{4.2}$$

where $C_F = 4/3$, $C_A = 3$, and $N_F T_F = 3/2$ for QCD. $K(t_2, \mathbf{x}; t_1, \mathbf{y})$ is a retarded propagator of a from t_1 to t_2 at the point, $x = y = 0$, where the parton a is produced by hard scattering. The propagator is associated with the light-cone Hamiltonian, which has the form [1]

$$H = \delta E(\mathbf{p}) - i\mathcal{C}_3, \tag{4.3}$$

where $\delta E(\mathbf{p})$ and $\mathcal{C}_3$ are given by [1]

$$\begin{aligned} \delta E(\mathbf{p}) &= \frac{p\mathbf{p}^2}{2k(p-k)} + \frac{m_b^2}{2k} + \frac{m_c^2}{2(p-k)} - \frac{m_a^2}{2p}, \\ \mathcal{C}_3(\mathbf{x}) &= \frac{C_b + C_c - C_a}{2} v_2(\mathbf{x}) + \frac{C_a + C_c - C_b}{2} v_2(\frac{k}{p}\mathbf{x}) + \frac{C_a + C_b - C_c}{2} v_2(\frac{p-k}{p}\mathbf{x}). \end{aligned} \tag{4.4}$$

m_a and C_a are respectively the thermal mass and the Casimir factor ($C_F = 4/3$ for quarks and $C_A = 3$ for gluons) of the parton a. $C_F v_2(\mathbf{x})$ is the dipole propagation amplitude per unit length for a $q\bar{q}$ pair. The (vac) term in the time integration corresponds to vacuum fluctuations.

In order to include the effect of finite formation time in the momentum-space AMY formalism, Eq. (4.1) was reformulated such that [1]

$$\frac{d\Gamma^{a}_{bc}(t)}{dk} \equiv \frac{P^{a(0)}_{bc}(x)}{\pi p} \times \mathrm{Re} \int_0^t dt_1 \int_{\mathbf{q},\mathbf{p}} \frac{i\mathbf{q}\cdot\mathbf{p}}{\delta E(\mathbf{q})} \mathcal{C}(t) K(t,\mathbf{q};t_1,\mathbf{p}). \tag{4.5}$$

$d\Gamma^{a}_{bc}(t)/dk$ is defined as the radiation rate and the time integration of Eq. (4.5) over t from 0 to ∞ yields dP/dk in Eq. (4.1). In momentum space, the time-dependent $\mathcal{C}(t)$ acts as the Boltzmann collisional operator [1]

$$\begin{aligned} \mathcal{C}\psi(\mathbf{p}) = \int_{\mathbf{q}} C(\mathbf{q}) \Bigg\{ & \frac{C_b + C_c - C_a}{2} \left[\psi(\mathbf{p}) - \psi(\mathbf{p}-\mathbf{q})\right] \\ & + \frac{C_a + C_c - C_b}{2} [\psi(\mathbf{p}) - \psi(\mathbf{p} + \frac{k}{p}\mathbf{q})] \\ & + \frac{C_a + C_b - C_c}{2} [\psi(\mathbf{p}) - \psi(\mathbf{p} + \frac{p-k}{p}\mathbf{q})] \Bigg\}, \end{aligned} \tag{4.6}$$

where $\psi(\mathbf{p})$ is a wave function on momentum space, and the function $C(\mathbf{q})$ is associated with the dipole amplitude [1]

$$v_2(\mathbf{x}) \equiv \int_{\mathbf{q}} C(\mathbf{q})(1 - e^{i\mathbf{q}\cdot\mathbf{x}}). \tag{4.7}$$

This can also be expressed in terms of the elastic collisional rate for a hard particle [1]

$$C(\mathbf{q}) = \frac{(2\pi)^2}{C_s} \frac{d\Gamma_{\mathrm{el}}(\mathbf{q})}{d^2 q}, \tag{4.8}$$

where the choice of $d\Gamma_{\mathrm{el}}/dk$ is

$$\frac{d\Gamma_{\mathrm{el}}(\mathbf{q})}{d^2 q} = \frac{g^2 m_D^2}{32\pi^2 q^3}, \tag{4.9}$$

which is taken from Ref. [86].

Eq. (4.5) contains a single time integration which can be solved numerically. The new time variable t represents the time of the last scattering between t_1 and t_2, where the next emission is supposed to occurs. Note that the time integration in Eq. (4.5) is evaluated up to finite t, unlike the AMY formulation in which time dependence is absent. The AMY rates are obtained by calculating feynman diagrams such as Fig. 2–7, which gives the total probability of radiation per total time, $dP_{\rm tot}/dT_{\rm tot}$. On the other hand, in this finite time formation, interference effects such as LPM effect are included in the propagator K, which is evaluated numerically.

The schematic diagram for the finite-size effect of a parton propagating through the QGP medium is depicted in Fig. 4–2. This figure illustrates the environment where the Eq. (4.5) is effective. A given parton of momentum $\mathbf{p}$ is broken into two bremsstrahlung partons with momenta $\mathbf{q}$ and $\mathbf{p}-\mathbf{q}$. The red lines represent hard parton propagators, either a quark or a gluon, species of which are arbitrary chosen. The black vertical gluon propagators with a shaded blob at each edge indicate not the additional bremsstrahlung emitted from the hard partons, but the multiple scatterings by thermal medium with soft momentum exchanges. Such collision processes directly induce the bremsstrahlung radiations. As can be seen in the figure, the emitted gluon as well as the mother quark undergo the multiple scatterings.

The mean free path of the scatterings with thermal medium, $l_{\rm mfp}$, is estimated in the following way. By definition,

$$\frac{1}{l_{\rm mfp}} \equiv \int d^3k\rho(k) \int dq^2(1-\cos\theta_{pk})\frac{d\sigma_{\rm el}}{dq^2}, \tag{4.10}$$

where $\rho(k)$ is the density of the thermal medium of momentum k ($\sim T$), and $(1 - \cos\theta_{pk})$ the flux factor with the angle θ_{pk} between the hard parton of momentum p and the thermal parton. The cross section for elastic scattering takes the form

$$\frac{d\sigma_{\rm el}}{d^2q} \sim C_R \frac{2\alpha_s^2}{(q^2)^2}. \tag{4.11}$$

With the debye mass $m_D^2 = \frac{3}{2}g^2T^2$ [1], Eq. (4.10) can be evaluated as

$$\begin{aligned}\frac{1}{l_{\rm mfp}} &\sim k^3 \int_{m_D^2}^{\infty} d^2q \frac{\alpha_s^2}{(q^2)^2} \\ &\sim T^3 \frac{\alpha_s^2}{m_D^2} \\ &\sim g^2 T,\end{aligned} \tag{4.12}$$

which yields

$$l_{\rm mfp} \sim \frac{1}{g^2T}. \tag{4.13}$$

The first emission from the mother quark occurs at time t_1 and the next splitting is located at time t, as it is in Eq. (4.5). The duration between t_1 and t corresponds to the formation time of the radiation. During the formation time, or within the coherence length, mother and daughter partons are considered to be in a coherent state and no further emission should exist. The separation condition imposed by the Heisenberg's uncertainty principle is such that the distance between the two partons $l_\perp$ is larger than the transverse size of the typical gluon:

$$l_\perp \gtrsim \frac{1}{q_\perp}, \tag{4.14}$$

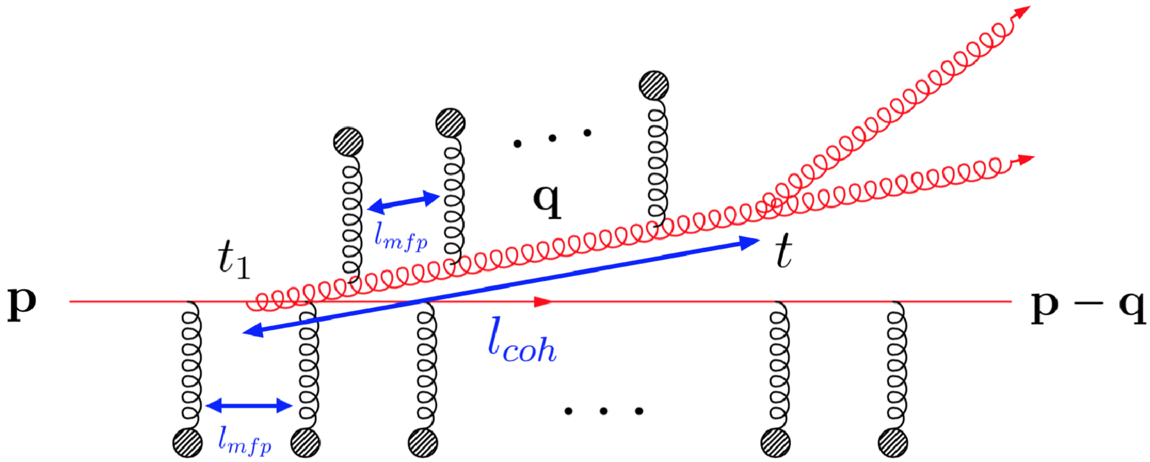

Figure 4–2: Schematic diagram for the finite-size effect of a parton propagating through the QGP medium. Hard partons are drown in red, while black curly lines with bulbs at the end of each represents soft scattering by the medium. A mother parton of momentum $\mathbf{p}$ and its daughter parton of momentum $\mathbf{q}$ are in a coherent state during the formation time, from t_1 to t, during which additional splitting is reduced.

where $\mathbf{q}_\perp$ is the transverse momentum of the daughter gluon relative to the mother quark and $q_\perp \equiv |\mathbf{q}_\perp|$. Let us derive the coherence length (time), $l_{\rm coh}$ in a heuristic approach. From the geometric relation,

$$\frac{q_\perp}{q} \sim \frac{l_\perp}{l_{\rm coh}}, \tag{4.15}$$

which yields with Eq. (4.14),

$$\begin{aligned} l_{\rm coh} &\sim \frac{q}{q_\perp} l_\perp \\ &\sim \frac{q}{(q_\perp)^2}. \end{aligned} \tag{4.16}$$

Now suppose that the emitted gluon of momentum $\mathbf{q}$ experiences N_{coh} soft scatterings with the transverse momentum transfer of μ^2 during the coherence length l_{coh}. Assuming that the motion of the gluon after each scattering follows a random walk and its transverse momentum $\mathbf{q}_\perp$ is determined by μ^2, we have

$$\left\langle (q_\perp)^2 \right\rangle = N_{\text{coh}}\mu^2 = \frac{l_{\text{coh}}}{l_{\text{mfp}}}\mu^2. \tag{4.17}$$

Using Eq.4.16 and the following definitions

$$\begin{aligned} \hat{q} &= \frac{\mu^2}{l_{\text{mfp}}}, \\ E_{\text{LPM}} &= \mu^2 l_{\text{mfp}}, \end{aligned} \tag{4.18}$$

l_{coh} becomes

$$l_{\text{coh}} \sim l_{\text{mfp}}\sqrt{\frac{q}{E_{\text{LPM}}}} = \sqrt{\frac{q}{\hat{q}}}. \tag{4.19}$$

In the absence of the formation time, the daughter gluon emitted at time t is considered to be fully separated from the mother quark and subsequent bremsstrahlung from both two partons is immediately possible.

The result of the numerical calculation of the Eq. (4.5), labelled with ‘Full’ is shown in Fig. 4–3 [1]. Comparison with results obtained from different prescriptions can also be seen in the figure. The radiation rate of AMY formalism doesn’t have any time dependence. This is because destructive interference between bremsstrahlung from hard partons and the vacuum radiation is not included in AMY as well as the formation time is not applicable. It begins to follow the full calculation roughly at the formation time, at which LPM interference between medium induced radiation starts to effective.

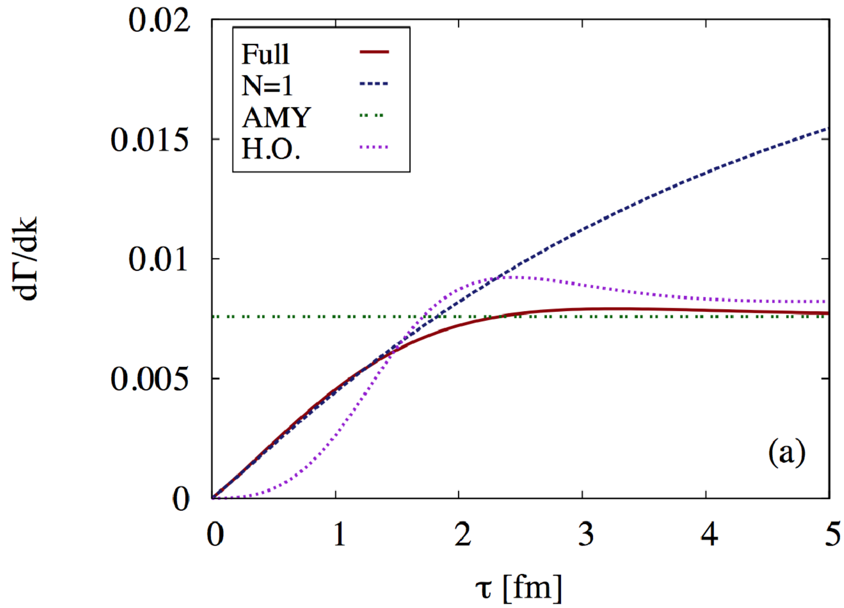

Figure 4–3: Radiation rate for a 3GeV gluon from 16GeV mother quark as a function of elapse time since the birth of the daughter gluon. Comparison between the results for the finite-size effect and other formalisms is made. In these calculations, couplings α_s are 0.3 and temperatures of the QGP medium are uniformly 0.2TeV [1].

On the other hand, the $N = 1$ approximation by the leading order opacity expansion [87, 88] closely coincides with the full calculation at the early time. N indicates the number of collisions that the hard partons experience during a formation time. The opacity expansion precisely follows 'Full' at the beginning, but single collision per coherence length overestimates the rates at later time due to the absence of the LPM effect.

Fig. 4–4 shows how MARTINI implements the radiative rate close to that proposed by [1]. In the Caron-Huot and Gale's calculation, a bump appears where the

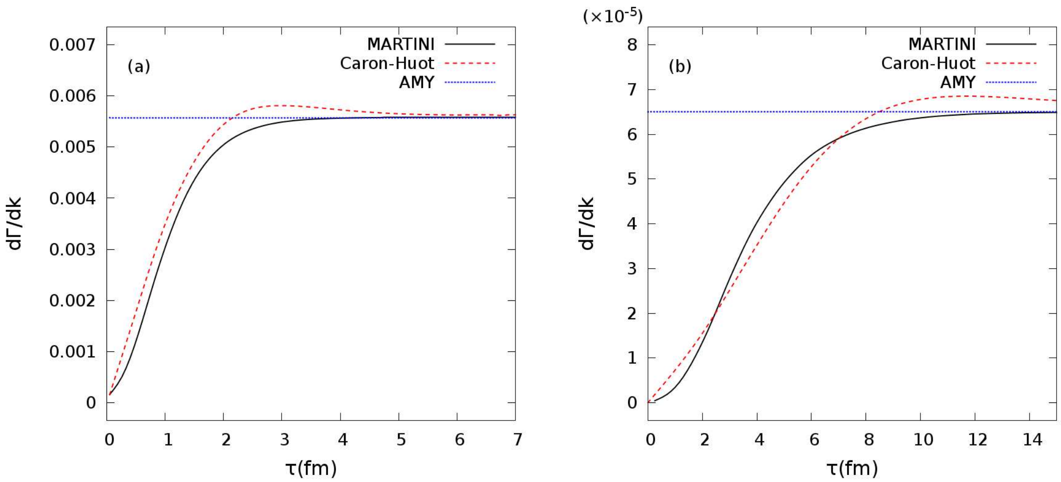

Figure 4–4: Radiation rate implemented in MARTINI, which is approximate to the Caron-Huot's calculation. (a) A 5GeV parton emitted from its mother parton of 50GeV. (b) A 100GeV parton radiated from a 300GeV parton. For both, temperatures are 0.4GeV and the coupling α_s is 0.3.

rate for the finite-size effect (red-dashed in Fig. 4–4) is above the AMY (blue-dotted) around the formation time.

We reproduced this modified rate as follows; we first generate a mother parton of momentum p and its daughter of k at a same position and let them move in the same z direction. Meanwhile, the two partons independently experience elastic processes, which alter the transverse momenta and positions of the particles. The separation condition of them is analogous to that in Eq. (4.14):

$$\Delta r_\perp > \frac{1}{2\Delta p_\perp}, \tag{4.20}$$

where $\Delta r_\perp$ and $\Delta p_\perp$ are differences between the positions and the transverse momenta, respectively, of the two partons. In each event, the moment when this condition first holds is recorded. The differential radiative rate $d\Gamma/dk$ is obtained by accumulating the momenum and normalized by both the number of events and the AMY rate. Comparison between MARTINI radiative rate and the original rate for finite-size effect as well as the AMY calculation are shown in Fig. 4–4. Fig. 4–4 (a) describes a gluon of 5GeV emitted from its mother quark of 50GeV, while (b) shows a 100GeV gluon radiated from a 300GeV quark at $T = 0.4$GeV and $\alpha_s = 0.3$. It can be seen that the approximated radiative rates in MARTINI (black-solid) smoothly connect to the AMY curve roughly after the formation time as expected.

4.1.2 Running Coupling

The strong coupling constant α_s in the previous version of MARTINI is chosen in accordance with a relevant energy scale examined in a simulation and is assumed to be a constant. However, as the energy scale increases, a deviation from the measured values of α_s appears. In order to determine the Q^2 dependence of the coupling α_s in MARTINI, the averaged transverse momentum transfer k_T in a splitting vertex is used. The estimated averaged k_T is given by [2]

$$\langle k_\perp^2 \rangle = \hat{q} t_f. \tag{4.21}$$

t_f indicates the formation time of an emission after scatterings with the medium. The jet transport coefficient $\hat{q}$ that appears in the expression can be derived from the equation in the fluid rest frame [89],

$$\hat{q} = \int^{q_{\max}} d^2 q_\perp q_\perp^2 \frac{d\Gamma_{\text{el}}}{d^2 q_\perp}, \tag{4.22}$$

where $q_{\max} \sim 6ET$ [89] is the UV cut-off. The hard thermal loop (HTL) re-summed elastic collision rate $d\Gamma_{\rm el}/d^2q_\perp$ is given by [89]

$$\frac{d\Gamma_{\rm el}}{d^2q_\perp} = \frac{C_a g^2 T}{(2\pi)^2} C(\mathbf{q}_\perp), \tag{4.23}$$

where expression for $C(\mathbf{q}_\perp)$ is shown in Eq. (2.17).

Using the expression shown in Eq. (4.16), Eq. (4.21) becomes

$$\langle k_\perp^2 \rangle = \hat{q} \frac{k}{\langle k_\perp^2 \rangle}, \tag{4.24}$$

which leads to [2]

$$\langle |k_\perp| \rangle = (\hat{q}k)^{\frac{1}{4}}. \tag{4.25}$$

The additional contribution of the coupling comes from the momentum transfer of soft scattering vertex, which is of order gT [2] and its running effect is not considered in this work.

Fig. 4–5 illustrates the running effect of α_s as a function of momentum p at temperature of 0.5GeV. The default coupling is set to 0.27 and it is assumed to start running at 10GeV. Below the reference momentum, the running effect is ignored. The running coupling shown as the black solid curve is compared to the default coupling of the red-dotted curve. A decrease of roughly 20% at 100GeV is obtained with the approximated calculation for running coupling.

The old results for the running coupling effects as well as the finite-size effect are shown in Fig. 4–6 [2]. It is found that the both effects lead to less suppression of jet quenching up to 100GeV. However, due to the lack of enough statistics, error bars for each curve are omitted. In comparison, in the previous study carried out

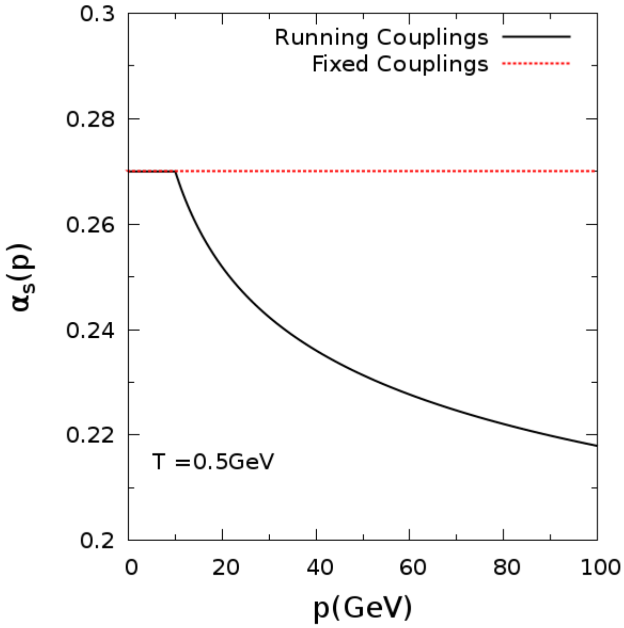

Figure 4–5: The running effect of a strong coupling constant α_s as a function of momentum p at temperature of 0.5GeV compared to a fixed coupling of 0.27. The effect starts at 10GeV and is ignored below the momentum.

in [2], the finite size effect was estimated, not actually calculated.

4.2 Monte Carlo Implementation

The main task of MARTINI is to solve the rate equation Eq. (3.11) using the Monte Carlo techniques in order to simulate the evolution of hard partons in the QGP medium, provided by equations of hydrodynamics. We shall follow the entire course of an event simulation generated by MARTINI.

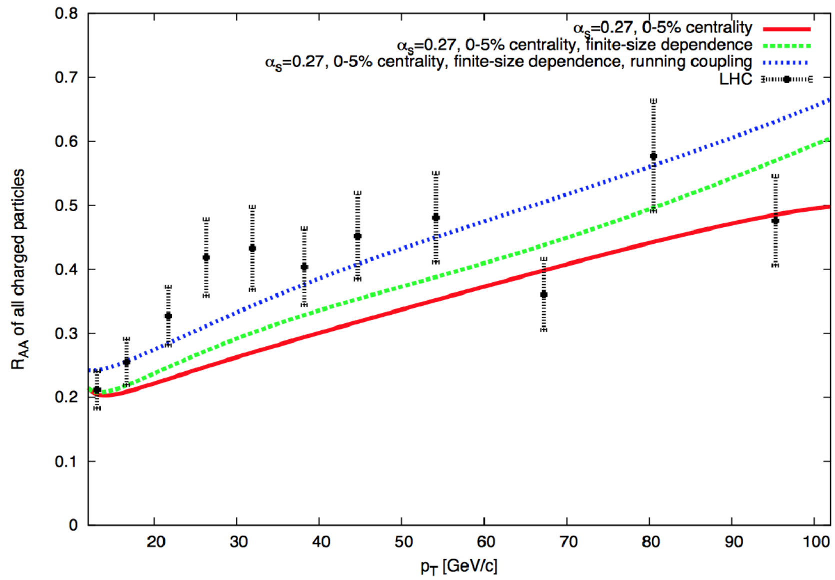

Figure 4–6: Previous results of the charged hadron R_{AA} with the finite-size effect and running coupling [2] compared with the preliminary CMS data.

The simulation begins with the creation of the nucleon-nucleon collisions by PYTHIA. The position of each initial hard process on the transverse plain is determined by the initial jet density distribution [49]:

$$\mathcal{P}_{AB}(b, \mathbf{r}_T) = \frac{T_A(\mathbf{r}_T + \mathbf{b}/2)T_B(\mathbf{r}_T - \mathbf{b}/2)}{T_{AB}(b)}, \tag{4.26}$$

which represents the collision of the nucleons A and B with the impact parameter $\mathbf{b}$, which originated from the Glauber model [90]. The nuclear thickness function of the nucleon A, $T_A(r)$ is given by [49, 90]

$$T_A(\mathbf{r}_T) = \int d^2z\rho_A(\mathbf{r}_T, z), \tag{4.27}$$

and the overlap function $T_{AB}(b)$ is defined as [49, 90]

$$T_{AB}(b) = \int d^2z T_A(\mathbf{r}_T) T_B(\mathbf{r}_T + \mathbf{b}) \tag{4.28}$$

In order to evaluate these functions, we used the Wood-Saxon form of the nuclear density function [49, 90]

$$\rho_A(\mathbf{r}) = \frac{\rho_0}{1 + \exp\left(\frac{r-R}{d}\right)}, \tag{4.29}$$

where $R = 6.38$fm is the radius of the gold nucleus, $d = 0.535$fm the surface depth parameter, which values are taken from [91]. The normalization factor ρ_0 is fixed to yield [49, 90]

$$\int d^3r \rho_A(\mathbf{r}) = A. \tag{4.30}$$

In practice, nucleons in the nuclei A and B are sampled using the Woods-Saxon distribution. MARTINI determines the overlap region using the impact parameter b and divides the area into circles with the inelastic cross-section σ_{inel} corresponding to the area, which forms a tube in 3–dimensions. Then the number of the binary collisions with the minimum jet transverse momentum p_T^{min} is determined within each tube using the number of nucleons in the tube from nucleus A and nucleus B. The probability for the jet events in each area is given by $\sigma_{\text{jet}}(p_T^{\text{min}})/\sigma_{\text{inel}}$ [49]. The species of the nucleons in the binary collisions are randomly determined by the number of nucleons corresponding to each species within one nucleus. Alternatively, MARTINI also provides an option for the Optical Glauber, in which one (averaged) binary collision per event is sampled using Eq. (4.26) with identical Glauber model described above. In this study we use the Optical Glauber model and leave the event-by-event background study for future.

The initial parton distribution function (PDF) can be chosen using the Les Houches Accord PDF (LHAPDF) [92] interface, an external package linked to PYTHIA. In addition, other PDFs can be also selected according to the parameterization of the given tune equipped with PYTHIA. We also include nuclear effects on the PDF such as showing effect. The EKS98 [66] and EPS08 [93] parameterizations are available in MARTINI.

Once the initial hard processes are generated, PYTHIA does the full parton shower, i.e., initial state radiation and final state radiation, until the soft background is formed at τ_0. This is a reasonable assumption because most of the parton shower take place before the formation of QGP medium, $\tau < \tau_0$. With the help of the finite-size effect [1], the interference between the vacuum shower and the medium created at τ_0 is implemented.

After τ_0, partons, created by the hard collisions and the consequent shower, evolve through the medium. Each parton is given its velocity at each time step and moves accordingly. During the in-medium evolution, they also lose their energy through the collisional and radiative processes. MARTINI performs a Lorentz-boost into the rest frame of a fluid cell from the position of a parton in order to determine the local temperature and the energy E of the parton and calculate the intrinsic transition rates.

A parton may have probabilities for several processes at the same time and one process is picked at any given time step according to its own weight, which is determined by the energy of the parton and the temperature of the cell where the parton is located. When these processes occur, MARTINI uses a rejection method to sample related quantities such as radiated or transferred energy for, respectively, radiative or collisional transition rates and transferred transverse momentum for scattering elastic collisions.

When the sampling is finished, MARTINI boosts the partons back to the lab frame and they either exit the medium or continue to travel the medium, repeating the energy loss processes. This repetition occurs until the energy of the partons in the rest frame fall down to the same order of the local temperature, $E \leq 4T$. This assumption is reasonable since the AMY formalism is based on the high- energy/temperature approximation where $E > T$. Meanwhile, the collisional and radiative transition also stops at the moment when the momentum of a parton falls below a certain minimum $p_{\min}$, which is typically chosen to 3GeV.

During the in-medium evolution, MARTINI keeps track all colour string information of partons in the medium. Once the parton evolution terminates, the complete information on the strings is sent to PYTHIA to perform fragmentation, which is based on the Lund fragmentation model, and the additional decay of unstable particles. The procedures of the event simulation are finished after hadronization is performed and a list of the final state particles with their properties is passed to MARTINI.

4.3 Results and Discussion

The leading hadron nuclear modification factor R_{AA} is a useful observable to quantify the jet quenching effect of high transverse momentum p_T final particles which escaped from the QGP medium. On the other hand, dijet imbalance should allow us to not only identify the partonic energy loss in the medium but also investigate the geometric properties of jet productions and their quenching.

This thesis can be regarded as a follow-up study to the earlier work done by C. Young, B. Schenke, S. Jeon, and C. Gale [2]. This section shows the new and improved results for the observables obtained using MARTINI. Comparisons between the results and the CMS experimental data corresponding to the observables are also presented. For each observable, the detailed descriptions for the simulation scheme, i.e., parameter setup, jet reconstructions, are mentioned.

4.3.1 Leading Hadron R_{AA}

We simulated PbPb collisions at centre of mass energy $\sqrt{s} = 2.76$TeV at 3 different centrality classes; $0-5\%$, $5-10\%$, and $10-30\%$. In order to calculate the leading hadron spectra of pp and PbPb collisions, we used the Tune 2C [94] in the PYTHIA parameter set. This tune, in which CTEQ 6L1 PDF is used, is designed to describe the CDF data. More detailed information can be found in [94]. The impact parameter b is taken to be an average impact parameter $\langle b \rangle$ based on the Optical Glauber model and calculated by Eq. (7) in [95]. To calculate $\langle b \rangle$ for each centrality, we used the values of the minimum and maximum impact parameter, respectively, $b_{\rm min}$ and $b_{\rm max}$ and the averaged nuclear overlap function $\langle T_{AA} \rangle$ taken from [3, 96]. Those geometric quantities including the average number of participating nucleons $\langle N_{\rm part} \rangle$ and binary nucleon-nucleon collisions $\langle N_{\rm coll} \rangle$ are shown in Table 4–1. The inelastic nucleon-nucleon cross section $\sigma_{\rm inel}^{NN} = 64 \pm 5$mb [3] at $\sqrt{s} = 2.76$TeV was used. The values of $\langle b \rangle$ for the three different centralities of $0-5\%$, $5-10\%$, and

Centrality bin %	$b_{\min}$ (fm)	$b_{\max}$ (fm)	$\langle N_{\text{part}}\rangle$	rms	$\langle N_{\text{coll}}\rangle$	rms	$\langle T_{AA}\rangle$ (1/mb)	rms (1/mb)
0 - 5	0.00	3.50	381 ± 2	19.2	1660 ± 130	166	25.9 ± 1.06	2.60
5 - 10	3.50	4.94	329 ± 3	22.5	1310 ± 110	168	20.5 ± 0.94	2.62
10 - 30	4.94	8.55	224 ± 4	45.9	745 ± 67	240	11.6 ± 0.67	3.75

Table 4–1: Table for the geometric quantities for PbPb collisions at $\sqrt{s} = 2.76$TeV at $0-5\%$, $5-10\%$, and $10-30\%$ centrality bins. The minimum $b_{\min}$ and maximum $b_{\max}$ impact parameter are taken from [96], and the average number of participating nucleons $\langle N_{\text{part}}\rangle$, binary nucleon-nucleon collisions $\langle N_{\text{coll}}\rangle$, and nuclear overlap function $\langle T_{AA}\rangle$, as well as corresponding r.m.s values are taken from [3].

$10-30\%$ are respectively 2.31fm, 4.23fm, and 6.85fm. Also the rapidity range of $|\eta| < 1.0$ was used.

The hydrodynamic background that we adopted was obtained from the (3+1) dimensional ideal fluid simulation of MUSIC [50]. The default strong coupling α_s was set to 0.27 and no modifications in the factorization or renormalization scale were made. For the simulations of PbPb collisions, we performed 3 different settings: (*i*) default setting in MARTINI, where the finite-size effect and running coupling are not included, (*ii*) the default one with only the finite-size effect is turned on, and (*iii*) both the finite-size effect and running coupling are included.

The p_T spectrum for charged particles for $|\eta| < 1.0$ in pp collisions at $\sqrt{s} =$ 2.76TeV is shown in the upper panel of Fig. 4–7. The red curve represents the theoretical calculation using PYTHIA, while the black dots corresponds to the CMS measurements with statistical error bars for comparison. For pp collisions, the statistical uncertainties of the PYTHIA results are ignored as less than 0.2% at 100GeV, and 0.08% at 10GeV. To reach the enough statistics up to 100GeV, we performed

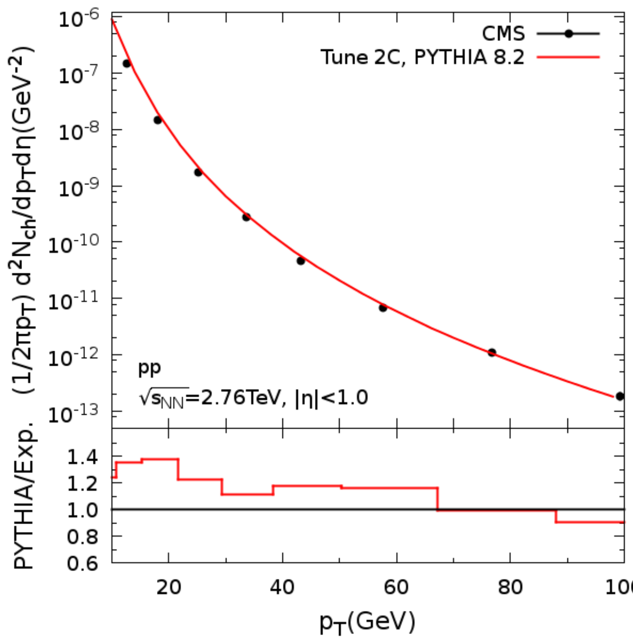

Figure 4–7: Upper panel : Invariant p_T distribution of charged particles in $\sqrt{s}$ = 2.76TeV pp collisions for $|\eta| < 1.0$. A PYTHIA tune used in this calculation is Tune 2C and the experimental measurement from the CMS is compared. Lower panel : The ratio of the PYTHIA simulation to the p_T spectrum obtained by the CMS [3].

independent simulations of 15 million PYTHIA events with identical parameters except $\hat{p}_T$ ranges. In PYTHIA, $\hat{p}_T$ constraints the kinematics of generated $2 \leftrightarrow 2$ processes and the range of $\hat{p}_T$ was divided into 5 sub-regions: $0-20$, $20-40$, $\cdots$, $80-100$GeV. Then we combined all sub-runs, which are weighted by the cross section for multiparton interactions where the kinematic constraints are applied. The lower panel shows the ratio between the PYTHIA simulation and the experimental measurement from the CMS. The ratio was obtained using power-law interpolation.

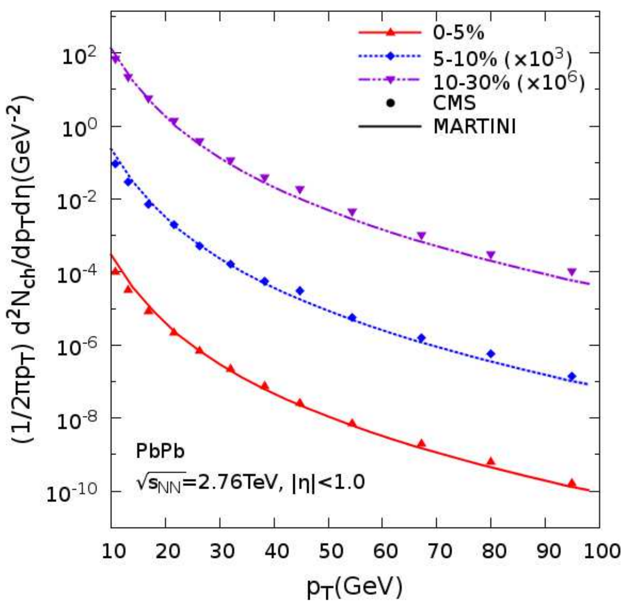

Figure 4–8: MARTINI results on the invariant p_T distribution of charged particles in $\sqrt{s} = 2.76$TeV pp collisions for $|\eta| < 1.0$. PYTHIA parameter set is same as in Fig. 4–7. Centrality classes of $0-5\%$ (red), $5-10\%$ (orange, $\times 10^3$), and $10-30\%$ (purple, $\times 10^6$) are calculated. For each class, an experimental measurement from the CMS data is compared [3].

The simulations for PbPb collisions at $\sqrt{s} = 2.76$TeV were performed using MARTINI and the results for the four different centrality bins are depicted in Fig. 4–8. In this calculation, we followed the same $\hat{p}_T$ cuts for each sub-runs as in pp cases, and 5 million events were generated in each centrality class and each sub-run. For visible comparison with the CMS data, p_T spectra for each centrality are multiplied by $\langle N_{coll} \rangle$ corresponding to the centrality classes, which is shown in Table. 4–1. The measurements from the CMS are represented by the dots, while the MARTINI results of the default settings are drawn by the lines. For both, their statistical uncertainties are included. Different colours indicate the different centrality classes:

the red, orange, and purple correspond $0-5\%$, $5-10\%$, and $10-30\%$ centralities, respectively.

Fig. 4–9 shows the charged particle nuclear modification factor R_{AA} as a function of transverse momentum p_T at different centrality bins. We sampled only one nucleon-nucleon collisions in one event when running MARTINI. That is, the MARTINI results represents the numerator of Eq. (4.31), while the denominator is obtained from PYTHIA.

$$R_{AA}(p_T) = \frac{(1/\langle N_{\rm coll}\rangle) d^2N^{AA}/dp_T d\eta}{d^2N^{pp}/dp_T d\eta} \tag{4.31}$$

Therefore, we directly divided the PbPb spectra by the pp reference without any scale modification.

The centrality dependence of the R_{AA} can be seen in Fig. 4–9 (a)-(c) for charged particles and (d)-(f) for negative pions. The left figures in each panel is the centrality bin for $0-5\%$, and the centre and right ones are those for $5-10\%$ and $10-30\%$ respectively. The red solid curves in each box depict the default setting (i), while the blue dot curves and green dashed-dot curves represent respectively the (ii) and (iii) scenarios. The error bars indicate the statistics uncertainties for each curve. We compared the results with the experimental measurements by the CMS [3], which are plotted as the black square with the systematic uncertainties of the grey shadows.

Significant fluctuations with uncorrelated p_T dependence of the statistical error bars in the CMS measurements are observed for more peripheral centralities. On the other hand, the MARTINI results show smooth curves for data points with high statistics correlated to p_T. Both the finite size and the running coupling effect lead

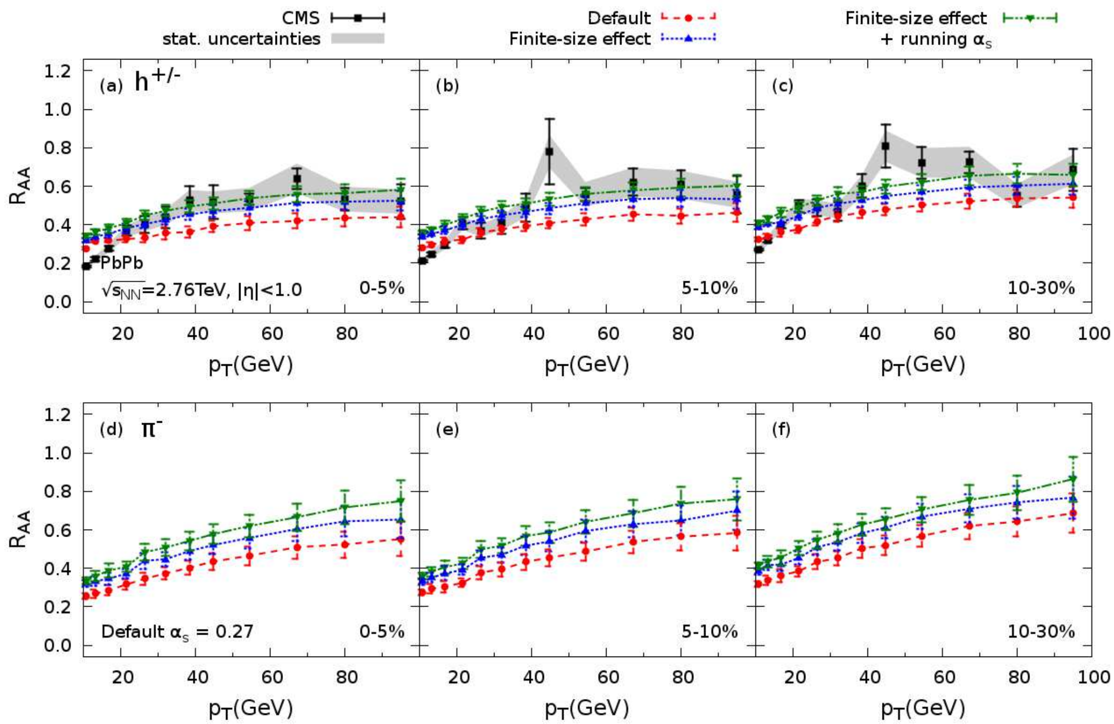

Figure 4–9: R_{AA} with the finite-size effect and running coupling at different centrality classes. Upper panel : The charged particle R_{AA} compared with the preliminary CMS data [3]. Lower panel : Those for negative pions π^-. From left to right centrality classes correspond to $0-5\%$, $5-10\%$, and $10-30\%$.

to less quenching at all the p_T regions. This is expected as both effects lowers the effective scattering rate. The three graphs in all centrality bins are fairly in good agreement with the CMS data, especially for higher p_T regions, within the statistical uncertainties. However, substantial gaps are found between the degrees of increase in each R_{AA}. The R_{AA} curves with the both effects show enough rises for all centrality classes, while those of the default scenario remain below the uncertainty bands for the CMS data. The increase is clearly shown in the R_{AA} curves for π^-, which are depicted in Fig. 4–9 (d)–(f). This indicates that the experimental results include the running coupling effect and the finite-size effect.

4.3.2 Dijet Asymmetry

In order to perform jet reconstruction in the PbPb collision simulations, we used the anti-k_T jet algorithm [97], which is built in the FastJet package [98]. In this algorithm, a jet is selected to a cone containing a cluster of particles within a radial parameter R. To sort out jets out of all particles, the following definition of distances between the particles is used [97]:

$$d_{ij} = \min(k_{ti}^{2p}, k_{tj}^{2p})\frac{\Delta_{ij}^2}{R^2}, \tag{4.32}$$

where d_{ij} is the distance between particles i and j, and k_{ti} the transverse momentum of the particles i. The Δ_{ij}^2 is given by [97]

$$\Delta_{ij}^2 = (\phi_i - \phi_j)^2 + (\eta_i - \eta_j)^2, \tag{4.33}$$

where ϕ_i and η_i are respectively the azimuth angle and rapidity of the particle i. The anti-k_T algorithm uses the value $p = -1$ [97] in Eq. (4.32). Jet selection starts with the minimum d_{ij}, which corresponds to the hardest particle and its neighbour close together. Then, particles within a given radius of R around the hard particle are added to form a cluster of jets. The procedures continue until no particles above a given kinematic threshold remain. Once all particles are clustered in cones of jets, we determine pairs of jets which directions of propagation are in opposite. The jet pairs are considered to be created by identical hard processes and the difference between distances each jet travels within the medium results in imbalance of a energy distribution of the dijet.

The distributions of dijet asymmetry obtained from PbPb collisions at $\sqrt{s} = 2.76$TeV as a function of dijet momentum balance A_J are shown in Fig. 4–10. The quantity for balance (imbalance) is defined as

$$A_J = \frac{p_{T,1} - p_{T,2}}{p_{T,1} + p_{T,2}}, \tag{4.34}$$

where $p_{T,1}$ is the momentum of a leading jet and $p_{T,2}$ that of a subleading jet. The subscription for the leading and subleading jet implies that A_J is always positive. The simulations were performed in four different centrality bins: $0-10\%$ (top left), $10-20\%$ (top right), $20-30\%$ (bottom left), $30-50\%$ (bottom right). The average impact parameters $\langle b \rangle$ are taken from [99], which values for each centrality bin are respectively 3.4fm, 6.0fm, 7.8fm, and 9.9fm. A good agreement was found with the cross-check calculations for $\langle b \rangle$ using Eq. (7) in [95]. In this analysis, jets were determined by the cone of radius $R = 0.5$ and the we sampled imbalanced dijets which leading jets and subleading jets have momenta of $p_{T.1} > 120$GeV and $p_{T.2} > 50$GeV, respectively. We also restricted the azimuthal angle between the near-side and away-side jets $\Delta\phi_{12}$ to be larger than $2/3\pi$ so that the high quality of dijet selection is ensured. Jets outside of the rapidity range $|\eta| < 2.0$ were ignored.

Again, we followed the three scenarios adopted for the R_{AA} analysis in order to be consistent in investigating the effects of the two models on dijet imbalance. The red dashed curves represents the default MARTINI setting (i), the blue dot and the

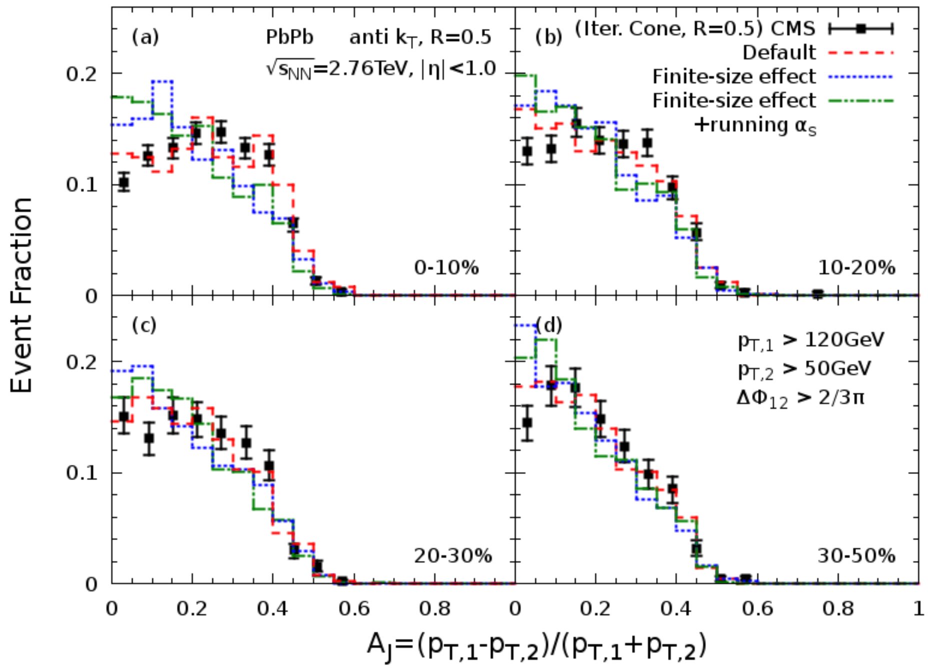

Figure 4–10: Dijet asymmetry with the finite-size effect and running coupling at different centrality classes. In the figure, (a)-(d) correspond to the results for the centrality of $0-10\%$, $10-20\%$, $20-30\%$, and $30-50\%$, respectively. The measurements from the CMS [99] are compared

green dashed double-dot one corresponds to respectively the default with the finite-size effect is added (*ii*) and the case both the models are turned on (*iii*). For dijet imbalance, we generated 500 thousands jet production events in each centrality class. The CMS measurements with the same kinematic cuts, taken from [99], are shown as the black squares with the statistical uncertainties. The iterative cone algorithm is used to define jets in the CMS measurements.

We find that both the effects influence on the results for dijet imbalance at all centralities. For the scenarios (*ii*) and (*iii*), sizeable enhancements of the dijet variable A_J are observed for $A_J < 0.2$, although the default modes are relatively in agreement with the CMS data. This indicates an underestimation of dijet imbalance, resulting from the use of the Optical Glauber approximation where no temperature fluctuation in the medium exists. Compared to the case of R_{AA}, the discrepancy is more noticeable in the dijet measurements which require plentiful information on the internal structure of the medium. This leaves potential to improve the jet simulations by introducing the event-by-event calculation and the IP-Glasma initial conditions where wider deflection of jets are expected to be observed due to the lumpiness of the medium.

CHAPTER 5
Conclusion

We have presented a theoretical and phenomenological study of jet quenching in relativistic heavy ion collisions using MARTINI, a Monte Carlo jet event generator. The essential aspect of this study is incorporation of the two models [1,2] improving the jet radiative energy loss mechanism into MARTINI.

The finite-size effect takes account of an energy-dependent formation time in an inelastic process. During the formation, the hard parton and the radiated parton are in a coherent state, in which additional emissions are suppressed. This also takes into account interference between vacuum radiation and that from hard partons occurring during the time. They lead to the gradually increasing radiative rate, which smoothly connects the flat region where the LPM effect is dominant. For the running coupling effect, we let α_s appearing in an emission vertex be a function of hard scale Q so that the radiative transition rates are directly affected.

Using the strong coupling $\alpha_s = 0.27$ in the infrared (IR) limit and the ideal (3+1) dimensional hydrodynamic background obtained from MUSIC, both the nuclear modification factor R_{AA} and dijet imbalance were well reproduced by MARTINI at different centralities. For R_{AA}, the effective rise from $0.2 \sim 0.4$ at 10GeV to $0.4 \sim 0.6$ at 100GeV confirmed that the particles of higher energy scale are less likely to lose their energy during the QGP evolution. We have also shown that the prescription for the finite formation time and running coupling reduces the jet quenching at all p_T regions.

In this work, we have treated the dynamics of the background soft medium as a ideal (3+1) dimensional hydrodynamics averaged over all events. This is the simplest case where no fluctuations of each binary collisions are visible. Although we mainly focused on the jet quenching behaviour at high-energy scale up to $p_T =$ 100GeV where such effects are weak, it is demanded to describe the QGP medium using more realistic models. In practice, event-by-event simulations including viscous hydrodynamics or imposing IP-Glasma initial conditions are crucial to describe the experimental measurements at a low p_T region. These medium fluctuations will be a good inspiration of our further study.

Under the pQCD prediction, the jet quenching in heavy ion collisions is expected to be weaker as a region of kinematics is expanded. For example, the effects of the formation time discussed in this study as well as running coupling, both of which have the energy dependence, would be significant at the higher energy scale. On the other hand, recent results from experiment collaborations such as ATLAS reveal the plateau-shaped leading hadron R_{AA} at higher p_T of few hundred GeV. Such a kinematic realm in which new treatment of the total energy loss rate is required should be investigated in future to determine the applicability of the two models and find good explanation of the jet quenching mechanism.

In conclusion, we have demonstrated that, with the two radiative energy loss mechanisms, MARTINI has enhanced capability for reproducing jet quenching phenomenon in heavy ion collisions using the ideal hydrodynamics. The future work will cover viscous hydrodynamics and IP-Glasma event-by-event simulation which contain initial fluctuation of nucleon positions. These initial conditions will lead to more realistic behaviour of the dijet pairs in the QGP medium and provide us with better description of dijet imbalance in heavy ion collisions.

REFERENCES

[1] S. Caron-Huot and C. Gale, Phys. Rev. **C82**, 064902 (2010), 1006.2379.

[2] C. Young, B. Schenke, S. Jeon, and C. Gale, Nucl. Phys. **A910-911**, 494 (2013), 1209.5679.

[3] CMS, S. Chatrchyan *et al.*, Eur. Phys. J. **C72**, 1945 (2012), 1202.2554.

[4] P. Huovinen, arXiv:nucl-th/0305064v1.

[5] H. Song, Eur. Phys. J. C (2012), arXiv:1207.2396 [nucl-th].

[6] L. D. Zanna *et al.*, Eur. Phys. J. C (2013), arXiv:1305.7052 [nucl-th].

[7] CMS Collaboration, C. Serguel *et al.*, Eur. Phys. J. C (2012), arXiv:1202.2554 [nucl-ex].

[8] ALICE Collaboration, B. B. Abelev *et al.*, Phys.Lett. **B736**, 196 (2014), arXiv:1401.1250 [nucl-ex].

[9] ALICE Collaboration, B. B. Abelev *et al.*, Eur.Phys.J. **C74**, 3108 (2014), arXiv:1405.3794 [nucl-ex].

[10] T. Renk, Phys.Rev. **C78**, 034904 (2008), arXiv:0803.0218 [hep-ph].

[11] T. Renk and K. Eskola, Phys.Rev. **C75**, 054910 (2007), hep-ph/0610059.

[12] STAR Collaboration, S. Salur, Eur.Phys.J. **C61**, 761 (2009), arXiv:0809.1609 [nucl-ex].

[13] PHENIX Collaboration, Y.-S. Lai, Nucl.Phys. **A830**, 251C (2009), arXiv:0907.4725 [nucl-ex].

[14] ATLAS Collaboration, G. Alexandre *et al.*, Physical Review Letters **105**, 052303 (2010).

[15] PHENIX Collaboration, S. Chatrchyan *et al.*, Physical Review C **84**, 024906 (2011).

[16] S.-L. Blyth *et al.*, J.Phys. **G34**, 271 (2007), nucl-ex/0609023.

[17] ALICE Collaboration, S. Aiola, J.Phys.Conf.Ser. **446**, 012005 (2013), arXiv:1304.6668 [nucl-ex].

[18] ATLAS Collaboration, G. Aad *et al.*, Phys.Rev.Lett. **114**, 072302 (2015), arXiv:1411.2357 [hep-ex].

[19] ALICE Collaboration, R. Haake, (2014), arXiv:1410.4437 [nucl-ex].

[20] ATLAS Collaboration, G. Aad *et al.*, Phys.Rev.Lett. **105**, 252303 (2010), arXiv:1011.6182 [hep-ex].

[21] CMS Collaboration, S. Chatrchyan *et al.*, Phys.Lett. **B712**, 176 (2012), arXiv:1202.5022 [nucl-ex].

[22] M. Gell-Mann, Physics Letters **8**, 214 (1964).

[23] G. Zweig, (1964).

[24] T. van Ritbergen, J. Vermaseren, and S. Larin, Phys.Lett. **B400**, 379 (1997), hep-ph/9701390.

[25] CMS, V. Khachatryan *et al.*, Eur. Phys. J. **C75**, 288 (2015), 1410.6765.

[26] K. G. Wilson, Phys. Rev. D **10**, 2445 (1974).

[27] O. Kaczmarek and F. Zantow, Phys. Rev. **D71**, 114510 (2005), hep-lat/0503017.

[28] O. Kaczmarek and F. Zantow, Eur. Phys. J. **C43**, 59 (2005), hep-lat/0502012.

[29] O. Kaczmarek and F. Zantow, (2005), hep-lat/0506019.

[30] E. Eichten *et al.*, Phys.Rev.Lett. **34**, 369 (1975).

[31] J. C. Collins and M. J. Perry, Phys. Rev. Lett. **34**, 1353 (1975).

[32] N. Cabibbo and G. Parisi, Physics Letters B **59**, 67 (1975).

[33] Y. Burnier, O. Kaczmarek, and A. Rothkopf, Phys. Rev. Lett. **114**, 082001 (2015).

[34] G. Martinez, (2013), arXiv:1304.1452 [nucl-ex].

[35] P. B. Arnold, G. D. Moore, and L. G. Yaffe, JHEP **0112**, 009 (2001), hep-ph/0111107.

[36] P. B. Arnold, G. D. Moore, and L. G. Yaffe, JHEP **0111**, 057 (2001), hep-ph/0109064.

[37] P. B. Arnold, G. D. Moore, and L. G. Yaffe, JHEP **0206**, 030 (2002), hep-ph/0204343.

[38] P. B. Arnold, G. D. Moore, and L. G. Yaffe, JHEP **0301**, 030 (2003), hep-ph/0209353.

[39] S. Turbide, C. Gale, S. Jeon, and G. D. Moore, Phys.Rev. **C72**, 014906 (2005), hep-ph/0502248.

[40] S. Jeon and G. D. Moore, Phys.Rev. **C71**, 034901 (2005), hep-ph/0309332.

[41] S. Jeon, Nucl. Phys. **A830**, 107C (2009), 0907.4691.

[42] P. Aurenche, F. Gelis, and H. Zaraket, JHEP **0205**, 043 (2002), hep-ph/0204146.

[43] G.-Y. Qin *et al.*, Phys.Rev.Lett. **100**, 072301 (2008), 0710.0605.

[44] B. Schenke, C. Gale, and G.-Y. Qin, Phys.Rev. **C79**, 054908 (2009), 0901.3498.

[45] T. Sjostrand, S. Mrenna, and P. Z. Skands, JHEP **05**, 026 (2006), hep-ph/0603175.

[46] T. Sjstrand *et al.*, Comput.Phys.Commun. **191**, 159 (2015), 1410.3012.

[47] B. Andersson, G. Gustafson, G. Ingelman, and T. Sjöstrand, Physics Reports **97**, 31 (1983).

[48] T. Sjöstrand, Nuclear Physics B **248**, 469 (1984).

[49] B. Schenke, C. Gale, and S. Jeon, Phys.Rev. **C80**, 054913 (2009), 0909.2037.

[50] B. Schenke, S. Jeon, and C. Gale, Phys.Rev. **C82**, 014903 (2010), 1004.1408.

[51] K. Eskola, H. Honkanen, H. Niemi, P. Ruuskanen, and S. Rasanen, Phys.Rev. **C72**, 044904 (2005), hep-ph/0506049.

[52] P. F. Kolb, J. Sollfrank, and U. W. Heinz, Phys.Rev. **C62**, 054909 (2000), hep-ph/0006129.

[53] P. F. Kolb and R. Rapp, Phys.Rev. **C67**, 044903 (2003), hep-ph/0210222.

[54] C. Nonaka and S. A. Bass, Phys.Rev. **C75**, 014902 (2007), nucl-th/0607018.

[55] U. W. Heinz, J. S. Moreland, and H. Song, Phys.Rev. **C80**, 061901 (2009), 0908.2617.

[56] E. Braaten and M. H. Thoma, Physical Review D **44**, 1298 (1991).

[57] E. Braaten and M. H. Thoma, Physical Review D **44**, 2625 (1991).

[58] J. Kapusta, P. Lichard, and D. Seibert, Phys. Rev. D **44**, 2774 (1991).

[59] R. Baier, H. Nakkagawa, A. Nigawa, and K. Redlich, Zeitschrift fr Physik C Particles and Fields **53**, 433 (1992).

[60] M. G. Mustafa, Phys.Rev. **C72**, 014905 (2005), hep-ph/0412402.

[61] M. G. Mustafa and M. H. Thoma, Acta Phys.Hung. **A22**, 93 (2005), hep-ph/0311168.

[62] E. Braaten and M. H. Thoma, Phys. Rev. **D44**, 1298 (1991).

[63] M. H. Thoma, Phys. Lett. **B273**, 128 (1991).

[64] PHENIX, S. S. Adler *et al.*, Phys. Rev. **C76**, 034904 (2007), nucl-ex/0611007.

[65] CTEQ, H. L. Lai *et al.*, Eur. Phys. J. **C12**, 375 (2000), hep-ph/9903282.

[66] K. J. Eskola, V. J. Kolhinen, and C. A. Salgado, Eur. Phys. J. **C9**, 61 (1999), hep-ph/9807297.

[67] P. F. Kolb and U. W. Heinz, (2003), nucl-th/0305084.

[68] A. Dainese, C. Loizides, and G. Paic, Eur. Phys. J. **C38**, 461 (2005), hep-ph/0406201.

[69] I. Vitev and M. Gyulassy, Phys. Rev. Lett. **89**, 252301 (2002), hep-ph/0209161.

[70] I. Vitev, J. Phys. **G30**, S791 (2004), hep-ph/0403089.

[71] C. A. Salgado and U. A. Wiedemann, Phys. Rev. **D68**, 014008 (2003), hep-ph/0302184.

[72] N. Armesto, A. Dainese, C. A. Salgado, and U. A. Wiedemann, Phys. Rev. **D71**, 054027 (2005), hep-ph/0501225.

[73] T. Renk, H. Holopainen, R. Paatelainen, and K. J. Eskola, Phys. Rev. **C84**, 014906 (2011), 1103.5308.

[74] ALICE, K. Aamodt *et al.*, Phys. Lett. **B696**, 30 (2011), 1012.1004.

[75] WA98, M. M. Aggarwal *et al.*, Eur. Phys. J. **C23**, 225 (2002), nucl-ex/0108006.

[76] D. G. d'Enterria, Phys. Lett. **B596**, 32 (2004), nucl-ex/0403055.

[77] PHENIX, A. Adare *et al.*, Phys. Rev. Lett. **101**, 232301 (2008), 0801.4020.

[78] STAR, J. Adams *et al.*, Phys. Rev. Lett. **91**, 172302 (2003), nucl-ex/0305015.

[79] B. G. Zakharov, JETP Lett. **63**, 952 (1996), hep-ph/9607440.

[80] B. G. Zakharov, JETP Lett. **65**, 615 (1997), hep-ph/9704255.

[81] V. N. Gribov and L. N. Lipatov, Sov. J. Nucl. Phys. **15**, 438 (1972), [Yad. Fiz.15,781(1972)].

[82] V. N. Gribov and L. N. Lipatov, Sov. J. Nucl. Phys. **15**, 675 (1972), [Yad. Fiz.15,1218(1972)].

[83] L. N. Lipatov, Sov. J. Nucl. Phys. **20**, 94 (1975), [Yad. Fiz.20,181(1974)].

[84] G. Altarelli and G. Parisi, Nuclear Physics B **126**, 298 (1977).

[85] Y. L. Dokshitzer, Sov. Phys. JETP **46**, 641 (1977), [Zh. Eksp. Teor. Fiz.73,1216(1977)].

[86] M. H. Thoma, Physics Letters B **273**, 128 (1991).

[87] M. Gyulassy, P. Levai, and I. Vitev, Nucl. Phys. **B571**, 197 (2000), hep-ph/9907461.

[88] M. Gyulassy, P. Levai, and I. Vitev, Nucl. Phys. **B594**, 371 (2001), nucl-th/0006010.

[89] JET, K. M. Burke *et al.*, Phys. Rev. **C90**, 014909 (2014), 1312.5003.

[90] R. Glauber *et al.*, Lectures in theoretical physics, 1959.

[91] C. De Jager, H. De Vries, and C. De Vries, Atomic data and nuclear data tables **14**, 479 (1974).

[92] M. R. Whalley, D. Bourilkov, and R. C. Group, The Les Houches accord PDFs (LHAPDF) and LHAGLUE, in *HERA and the LHC: A Workshop on the implications of HERA for LHC physics. Proceedings, Part B*, 2005, hep-ph/0508110.

[93] K. J. Eskola, H. Paukkunen, and C. A. Salgado, JHEP **07**, 102 (2008), 0802.0139.

[94] R. Corke and T. Sjostrand, JHEP **03**, 032 (2011), 1011.1759.

[95] H. Niemi, K. J. Eskola, and P. V. Ruuskanen, Phys. Rev. **C79**, 024903 (2009), 0806.1116.

[96] B. Abelev *et al.*, Physical Review C **88**, 044909 (2013).

[97] M. Cacciari, G. P. Salam, and G. Soyez, JHEP **04**, 063 (2008), 0802.1189.

[98] M. Cacciari, FastJet: A Code for fast k_t clustering, and more, in *Deep inelastic scattering. Proceedings, 14th International Workshop, DIS 2006, Tsukuba, Japan, April 20-24, 2006*, pp. 487–490, 2006, hep-ph/0607071, [,487(2006)].

[99] CMS, S. Chatrchyan *et al.*, Phys. Rev. **C84**, 024906 (2011), 1102.1957.